J. Fluid Mech. (2020), *vol*. 905, A8. © The Author(s), 2020.
Published by Cambridge University Press
doi:10.1017/jfm.2020.711

Transport phenomena in fluid films with curvature elasticity

Arijit Mahapatra[1], **David Saintillan**[1] **and Padmini Rangamani**[1],†

[1]Department of Mechanical and Aerospace Engineering, University of California San Diego, 9500 Gilman Drive, La Jolla, CA 92093, USA

(Received 16 January 2020; revised 22 June 2020; accepted 31 July 2020)

Cellular membranes are elastic lipid bilayers that contain a variety of proteins, including ion channels, receptors and scaffolding proteins. These proteins are known to diffuse in the plane of the membrane and to influence the bending of the membrane. Experiments have shown that lipid flow in the plane of the membrane is closely coupled with the diffusion of proteins. Thus, there is a need for a comprehensive framework that accounts for the interplay between these processes. Here, we present a theory for the coupled in-plane viscous flow of lipids, diffusion of transmembrane proteins and elastic deformation of lipid bilayers. The proteins in the membrane are modelled such that they influence membrane bending by inducing a spontaneous curvature. We formulate the free energy of the membrane with a Helfrich-like curvature elastic energy density function modified to account for the chemical potential energy of proteins. We derive the conservation laws and equations of motion for this system. Finally, we present results from dimensional analysis and numerical simulations and demonstrate the effect of coupled transport processes in governing the dynamics of membrane bending and protein diffusion.

Key words: membranes, thin films, capsule/cell dynamics

1. Introduction

Lipid bilayers are present both in the plasma membrane and in intracellular organelles (Alberts *et al.* 1985) and have an extremely heterogeneous composition (Harayama & Riezman 2018). They consist of many different types of lipids, integral and peripheral membrane proteins (Bassereau *et al.* 2018), all of which are important in cellular function (Singer 1974). One of the classic features of cellular membranes is their ability to bend out of plane and this has been the focus of many studies, both theoretical and experimental, over the past five decades (Sackmann, Duwe & Engelhardt 1986; Lipowsky 1991; Jülicher & Lipowsky 1993; Zimmerberg & Kozlov 2006; Hassinger *et al.* 2017). We now also know that these membrane–protein interactions in cells are associated with many curvature sensing (Antonny 2011) and curvature generating phenomena (McMahon & Gallop 2005) including tubulation (Stachowiak, Hayden & Saski 2010), vesicle generation (Reynwar *et al.* 2007) and membrane trafficking (Mujherjee & Maxfield 2000; Gruenberg 2001). Curvature is a shape variable of the membrane that is related to the internal parameters such as protein density, tilt angle,

† Email address for correspondence: prangamani@ucsd.edu

J. Fluid Mech. (2020), *vol*. 905, A8. © The Author(s), 2020.
Published by Cambridge University Press
doi:10.1017/jfm.2020.711

Transport phenomena in fluid films with curvature elasticity

Arijit Mahapatra[1], **David Saintillan**[1] **and Padmini Rangamani**[1],†

[1]Department of Mechanical and Aerospace Engineering, University of California San Diego, 9500 Gilman Drive, La Jolla, CA 92093, USA

(Received 16 January 2020; revised 22 June 2020; accepted 31 July 2020)

Cellular membranes are elastic lipid bilayers that contain a variety of proteins, including ion channels, receptors and scaffolding proteins. These proteins are known to diffuse in the plane of the membrane and to influence the bending of the membrane. Experiments have shown that lipid flow in the plane of the membrane is closely coupled with the diffusion of proteins. Thus, there is a need for a comprehensive framework that accounts for the interplay between these processes. Here, we present a theory for the coupled in-plane viscous flow of lipids, diffusion of transmembrane proteins and elastic deformation of lipid bilayers. The proteins in the membrane are modelled such that they influence membrane bending by inducing a spontaneous curvature. We formulate the free energy of the membrane with a Helfrich-like curvature elastic energy density function modified to account for the chemical potential energy of proteins. We derive the conservation laws and equations of motion for this system. Finally, we present results from dimensional analysis and numerical simulations and demonstrate the effect of coupled transport processes in governing the dynamics of membrane bending and protein diffusion.

Key words: membranes, thin films, capsule/cell dynamics

1. Introduction

Lipid bilayers are present both in the plasma membrane and in intracellular organelles (Alberts *et al.* 1985) and have an extremely heterogeneous composition (Harayama & Riezman 2018). They consist of many different types of lipids, integral and peripheral membrane proteins (Bassereau *et al.* 2018), all of which are important in cellular function (Singer 1974). One of the classic features of cellular membranes is their ability to bend out of plane and this has been the focus of many studies, both theoretical and experimental, over the past five decades (Sackmann, Duwe & Engelhardt 1986; Lipowsky 1991; Jülicher & Lipowsky 1993; Zimmerberg & Kozlov 2006; Hassinger *et al.* 2017). We now also know that these membrane–protein interactions in cells are associated with many curvature sensing (Antonny 2011) and curvature generating phenomena (McMahon & Gallop 2005) including tubulation (Stachowiak, Hayden & Saski 2010), vesicle generation (Reynwar *et al.* 2007) and membrane trafficking (Mujherjee & Maxfield 2000; Gruenberg 2001). Curvature is a shape variable of the membrane that is related to the internal parameters such as protein density, tilt angle,

† Email address for correspondence: prangamani@ucsd.edu

local composition (Leibler & Andelman 1987) and intermonolayer differences of the membrane (Seifert 1993). Proteins embedded in the membrane diffuse in the plane of the membrane and undergo transport by advection processes (Kahya *et al.* 2004) associated with viscous flow of the lipids (Tran-Son-Tay, Sutera & Rao 1984; Noguchi & Gompper 2004). Experimental observations in reconstituted or synthetic lipid vesicles show that the coupling of lipid flow, protein diffusion and membrane bending can give rise to emergent phenomena (Baumgart, Hess & Webb 2003; Horner, Antonenko & Pohl 2009; Snead *et al.* 2017). There are theoretical models that have explicitly studied the coupling between concentration of curvature-inducing proteins and the bending of the membrane (Lowengrub, Ratz & Voigt 2009; Elliott & Stinner 2013; Elliott *et al.* 2016) and coupling between viscous flow and bending (Seifert & Langer 1993). The coupling between flow, diffusion and bending has not been commonly considered with the exception of a few phase transition models (Sahu, Sauer & Mandadapu 2017). Thus, there is a need to understand how the interplay of protein diffusion, lipid flow, and membrane bending determines the mechanical response of lipid bilayers.

The seminal work of Helfrich (1973), Canham (1970) and Jenkins (1977) established the framework for using variational principles and thin shell mechanics for modelling membrane bending. Later, Steigmann (1999) established the correspondence between Koiter's shell theory and developed a complete theoretical framework of membrane mechanics. These early models assumed the membrane to be inviscid and focused primarily on elastic effects. In the past decade, many groups have proposed the addition of viscous effects in addition to membrane bending (Arroyo & DeSimone 2009; Rahimi & Arroyo 2012; Rangamani *et al.* 2013; Tozzi, Walani & Arroyo 2019) building on the ideas proposed by Scriven (1960). We also showed recently that including intrasurface viscosity in addition to membrane bending allows for the calculation of local membrane tension in the presence of protein-induced spontaneous curvature (Rangamani, Mandadapu & Oster 2014) and for the calculation of flow fields on minimal surfaces (Bahmani, Christenson & Rangamani 2016). Separately, the interaction between in-plane protein diffusion and membrane bending has been modelled (Iglič *et al.* 2005; Kralj-Iglič *et al.* 2005; Ramaswamy, Toner & Prost 2005; Reynwar *et al.* 2007; Veksler & Gov 2007; Gozdz 2011). Specifically, Steigmann & Agrawal (2011) proposed a framework that included the chemical potential energy of membrane–protein interactions and membrane bending and demonstrated the interaction between bending and diffusion. A series of studies by Arroyo and coworkers also developed a comprehensive framework for incorporating membrane–protein interactions using Onsager's variational principles (Arroyo *et al.* 2018; Torres-Sanchez, Millan & Arroyo 2019; Tozzi *et al.* 2019).

Building on these efforts, we present a coupled theory for membrane mechanics that accounts for in-plane viscous flows and diffusion of curvature-inducing transmembrane proteins in addition to membrane bending. We note that a version of this model was presented by Steigmann (2018). Using a free energy functional that includes bending energy, chemical potential energy of membrane–protein interactions and, by including the viscous stresses in the force balance, we derive the governing equations of motion in § 2. In § 3.1, we analyse this system of equations assuming small deformations from the flat plane and identify the role of different dimensionless groups in governing the regimes of operation. We then perform numerical simulations in a one-dimensional model in § 3.2 and in a two-dimensional Monge parametrization in § 3.3. The case of large deformations is addressed in § 4 where we investigate the flattening of a membrane bud in axisymmetric coordinates. These results are cast in perspective of the current knowledge of the field and future directions are presented in § 5.

Notation	Description	Units
γ	Lagrange multiplier for incompressibility	$\mathrm{pN \cdot nm^{-1}}$
p	Pressure difference across the membrane	$\mathrm{pN \cdot nm^{-2}}$
C	Protein-induced spontaneous curvature	$\mathrm{nm^{-1}}$
θ^α	Surface coordinates	
W	Local free energy per unit area	$\mathrm{pN \cdot nm^{-1}}$
λ	Membrane tension, $\lambda = -(W + \gamma)$	$\mathrm{pN \cdot nm^{-1}}$
λ_0	Membrane tension at infinity	$\mathrm{pN \cdot nm^{-1}}$
$\zeta^{\alpha\beta}$	Elastic stress tensor	$\mathrm{pN \cdot nm^{-1}}$
$\pi^{\alpha\beta}$	Viscous deviatoric stress	$\mathrm{pN \cdot nm^{-1}}$
H	Mean curvature of the membrane	$\mathrm{nm^{-1}}$
K	Gaussian curvature of the membrane	$\mathrm{nm^{-2}}$
k	Bending modulus (rigidity)	$\mathrm{pN \cdot nm}$
$\bar{k}$	Gaussian modulus	$\mathrm{pN \cdot nm}$
σ	Protein density per unit area	$\mathrm{nm^{-2}}$
σ_s	Saturation protein density per unit area	$\mathrm{nm^{-2}}$
ℓ	Proportionality constant of $C - \sigma$ relation	nm
D	Protein diffusion coefficient, $D = k_B T/f$	$\mathrm{nm^2 \cdot s^{-1}}$
f	Hydrodynamic drag coefficient of a protein	$\mathrm{pN \cdot s \cdot nm^{-1}}$
L	Size of the domain	nm
k_B	Boltzmann constant	$\mathrm{pN \cdot nm \cdot K^{-1}}$
T	Temperature	K

TABLE 1. Summary of the notation used in the model.

2. Membranes with intra-surface viscosity and protein diffusion

We formulate the governing equations for the dynamics of an elastic lipid membrane with surface flow, coupled to the transport of membrane-embedded proteins that induce spontaneous mean curvature. We assume familiarity with tensor analysis and curvilinear coordinate systems (Sokolnikoff 1951; Kreyszig 1968; Aris 1989).

2.1. *Membrane geometry, kinematics and incompressibility*

The lipid membrane is idealized as a two-dimensional manifold Ω in three-dimensional space. Material points on Ω are parametrized by a position field $\boldsymbol{r}(\theta^\alpha, t)$, where θ^α are surface coordinates and play a role analogous to that of a fixed coordinate system used to parametrize a control volume in the Eulerian description of classical fluid mechanics. Here and henceforth, Greek indices range over $\{1, 2\}$ and, if repeated, are summed over that range. The local tangent basis on the surface is naturally obtained as $\boldsymbol{a}_\alpha = \boldsymbol{r}_{,\alpha}$ where commas identify partial derivatives with respect to θ^α. The unit normal field is then given by $\boldsymbol{n} = \boldsymbol{a}_1 \times \boldsymbol{a}_2/|\boldsymbol{a}_1 \times \boldsymbol{a}_2|$. The tangent basis also defines the surface metric $a_{\alpha\beta} = \boldsymbol{a}_\alpha \cdot \boldsymbol{a}_\beta$ (or coefficients of the first fundamental form), a positive definite matrix, which is one of the two basic variables in surface theory. The other is the curvature $b_{\alpha\beta}$ (or coefficients of the second fundamental form) defined as $b_{\alpha\beta} = \boldsymbol{n} \cdot \boldsymbol{r}_{,\alpha\beta}$. Of special interest are the mean ($\mathrm{nm^{-1}}$) and Gaussian ($\mathrm{nm^{-2}}$) curvatures, which will enter the Helfrich energy of the membrane and are defined, respectively, as

$$H = \tfrac{1}{2} a^{\alpha\beta} b_{\alpha\beta}, \quad K = \tfrac{1}{2} \varepsilon^{\alpha\beta} \varepsilon^{\mu\eta} b_{\alpha\mu} b_{\beta\eta}. \tag{2.1a,b}$$

Here, $a^{\alpha\beta} = (a_{\alpha\beta})^{-1}$ is the dual metric, and $\varepsilon^{\alpha\beta}$ is the permutation tensor defined as $\varepsilon^{12} = -\varepsilon^{21} = 1/\sqrt{a}$, $\varepsilon^{11} = \varepsilon^{22} = 0$.

We assume that the surface Ω is moving with time, and the velocity of a material point in the membrane is given by $\boldsymbol{u}(\theta^\alpha, t) = \dot{\boldsymbol{r}} = \partial \boldsymbol{r}/\partial t$. It can be expressed in components on the natural basis introduced above

$$\boldsymbol{u} = v^\alpha \boldsymbol{a}_\alpha + w\boldsymbol{n}, \tag{2.2}$$

where the components v^α capture the tangential lipid flow and w is the normal surface velocity. The membrane is assumed to be incompressible, which prescribes a relationship between the in-plane velocity field and the curvature as (Arroyo & DeSimone 2009; Rangamani *et al.* 2013)

$$v^\alpha_{;\alpha} = 2Hw, \tag{2.3}$$

where the semi-colon refers to covariant differentiation with respect to the metric $a_{\alpha\beta}$.

2.2. *Stress balance and equations of motion*

We model the membrane as a thin elastic shell and, in the absence of inertia, the equations of motion are the equations of mechanical equilibrium. For a membrane subjected to a lateral pressure difference p (pN $\cdot$ nm^{-2}) in the direction of the unit normal $\boldsymbol{n}$, these may be summarized as (Steigmann 1999)

$$\boldsymbol{T}^\alpha_{;\alpha} + p\boldsymbol{n} = \boldsymbol{0}, \tag{2.4}$$

where $\boldsymbol{T}^\alpha$ are the so-called stress vectors. The differential operation in (2.4) is the surface divergence

$$\boldsymbol{T}^\alpha_{;\alpha} = (\sqrt{a})^{-1}(\sqrt{a}\boldsymbol{T}^\alpha)_{,\alpha}, \tag{2.5}$$

where $a = \det(a_{\alpha\beta}) > 0$. This framework encompasses all elastic surfaces for which the energy density responds to metric and curvature. For example, if the energy density per unit mass of the surface is $F(a_{\alpha\beta}, b_{\alpha\beta})$, then (Steigmann 1999)

$$\boldsymbol{T}^\alpha = N^{\beta\alpha}\boldsymbol{a}_\beta + S^\alpha \boldsymbol{n}, \tag{2.6}$$

where

$$N^{\beta\alpha} = \zeta^{\beta\alpha} + \pi^{\beta\alpha} + b^\beta_\mu M^{\mu\alpha} \quad \text{and} \quad S^\alpha = -M^{\alpha\beta}_{;\beta}. \tag{2.7a,b}$$

We have introduced the notation $b^\alpha_\beta = a^{\alpha\lambda}b_{\lambda\beta}$. In (2.7*a*,*b*), $\zeta^{\beta\alpha}$ (pN $\cdot$ nm^{-1}) is the in-plane elastic stress tensor, $\pi^{\beta\alpha}$ (pN $\cdot$ nm^{-1}) is the intra-membrane viscous stress tensor due to surface flow and $M^{\alpha\beta}$ is the moment tensor due to curvature-induced elastic bending. We discuss constitutive equations for these various contributions in the next sections.

Substituting (2.6) and (2.7*a*,*b*) into (2.4), invoking the Gauss and Weingarten equations $\boldsymbol{a}_{\beta;\alpha} = b_{\beta\alpha}\boldsymbol{n}$ and $\boldsymbol{n}_{,\alpha} = -b^\beta_\alpha \boldsymbol{a}_\beta$ (Sokolnikoff 1951) and projecting the result onto the tangent and normal spaces of Ω provides the three governing equations

$$N^{\beta\alpha}_{;\alpha} - S^\alpha b^\beta_\alpha = 0, \quad S^\alpha_{;\alpha} + N^{\beta\alpha}b_{\beta\alpha} + p = 0, \tag{2.8a,b}$$

which express stress balances in the tangential and normal directions.

2.3. *Free energy of an elastic membrane with curvature-inducing proteins*

The elastic contribution of the surface stress and the moment tensor are derived from a free energy and are expressed as (Steigmann 1999)

$$\zeta^{\beta\alpha} = \rho\left(\frac{\partial F}{\partial a_{\alpha\beta}} + \frac{\partial F}{\partial a_{\beta\alpha}}\right), \quad M^{\alpha\beta} = \frac{\rho}{2}\left(\frac{\partial F}{\partial b_{\alpha\beta}} + \frac{\partial F}{\partial b_{\beta\alpha}}\right). \tag{2.9a,b}$$

Here, F is the energy Lagrangian per unit mass defined as (Steigmann 1999)

$$F(H, K, \rho) = \bar{F}(H, K) - \gamma/\rho, \tag{2.10}$$

where γ is a Lagrange multiplier imposing the constraint of incompressibility, and ρ is the membrane density which is assumed to be constant. It is customary to formulate the mechanics in terms of the free energy per unit area as (Steigmann *et al.* 2003)

$$W = \rho\bar{F}. \tag{2.11}$$

For an elastic membrane with a density σ (nm^{-2}) of curvature-inducing proteins, we model this free energy ($\mathrm{pN}\cdot\mathrm{nm}^{-1}$) as the sum of elastic and chemical energies (Veksler & Gov 2007; Steigmann & Agrawal 2011; Alimohamadi & Rangamani 2018)

$$W(H, K, \sigma) = k[H - C(\sigma)]^2 + \bar{k}K + k_BT\sigma\left[\log\left(\frac{\sigma}{\sigma_s}\right) - 1\right]. \tag{2.12}$$

The first two terms correspond to the classical Helfrich free energy and involve the two bending moduli k ($\mathrm{pN}\cdot\mathrm{nm}$) and $\bar{k}$ ($\mathrm{pN}\cdot\mathrm{nm}$). While these could in general depend on σ, we take them to be constant as is appropriate in the dilute limit. $C(\sigma)$ (nm^{-1}) is the protein-induced spontaneous curvature and is assumed to depend linearly on protein density (Veksler & Gov 2007; Steigmann & Agrawal 2011; Gov 2018)

$$C = \ell\sigma, \tag{2.13}$$

where the constant ℓ (nm) is a characteristic length scale associated with the embedded protein. The last term in (2.12) is the entropic contribution due to thermal diffusion of proteins (Gov 2018), where k_BT ($\mathrm{pN}\cdot\mathrm{nm}$) is the thermal energy and σ_s (nm^{-2}) denotes the saturation density of proteins on the membrane.

Inserting (2.12) for the free energy into (2.9*a*,*b*) provides expressions for the elastic stress and moment tensors as

$$\zeta^{\alpha\beta} = -2k(H - \ell\sigma)b^{\alpha\beta} - 2\bar{k}Ka^{\alpha\beta} - \gamma a^{\alpha\beta}, \tag{2.14}$$

$$M^{\alpha\beta} = k(H - \ell\sigma)a^{\alpha\beta} + \bar{k}(2Ha^{\alpha\beta} - b^{\alpha\beta}). \tag{2.15}$$

2.4. *Viscous stress*

In the presence of surface flow, a viscous stress also develops in the membrane. The deviatoric part of the viscous stress tensor $\pi^{\alpha\beta}$ is assumed to depend linearly on strain rate as (Scriven 1960)

$$\pi^{\alpha\beta} = \nu a^{\alpha\mu}a^{\beta\eta}\dot{a}_{\mu\eta}, \tag{2.16}$$

where ν, a positive constant, is the intra-membrane surface viscosity. Further expanding this expression, we obtain

$$\pi^{\alpha\beta} = 2\nu[a^{\alpha\mu}a^{\beta\eta}d_{\mu\eta} - wb^{\alpha\beta}], \tag{2.17}$$

where $d_{\mu\eta} = (v_{\mu;\eta} + v_{\eta;\mu})/2$ is the surface rate-of-strain tensor.

2.5. *Conservation equation for protein transport*

To complete the model, we specify a transport equation for the protein density σ. Mass conservation can be expressed as

$$\frac{\partial \sigma}{\partial t} + m^{\alpha}_{;\alpha} = 0, \tag{2.18}$$

where m^{α} denotes the protein flux. This flux has contributions from advection by the surface flow as well as from gradients in chemical potential. Following Steigmann & Agrawal (2011), it can be derived from first principles as

$$m^{\alpha} = \left[v^{\alpha} - \frac{1}{f} a^{\alpha\beta} W_{\sigma,\beta} \right] \sigma, \tag{2.19}$$

where f (pN $\cdot$ s $\cdot$ nm^{-1}) is the hydrodynamic drag coefficient of a protein and $W_{\sigma} = \partial W/\partial \sigma$.

2.6. *Summary of the governing equations*

We summarize the governing equations for the membrane and protein dynamics. The tangential momentum balance, obtained by inserting (2.14), (2.15) and (2.17) for the stresses into equation (2.8*a*), is expressed as

$$\lambda_{,\alpha} - 4\nu w H_{,\alpha} + 2\nu(a^{\beta\mu} d_{\alpha\mu;\beta} - w_{,\beta} b^{\beta}_{\alpha}) = -\sigma_{,\alpha} \left[k_B T \log\left(\frac{\sigma}{\sigma_s}\right) - 2k\ell(H - \ell\sigma) \right], \tag{2.20}$$

where we have introduced the membrane tension (pN $\cdot$ nm^{-1}) $\lambda = -(W + \gamma)$. Along with the surface incompressibility condition

$$v^{\alpha}_{;\alpha} - 2wH = 0, \tag{2.21}$$

(2.20) constitutes the governing equation for the intra-membrane flow. We note the similarity with the Stokes equations, where the tension λ plays a role analogous to the pressure in classical incompressible flow (Bahmani *et al.* 2016). The right-hand side captures the forcing by the protein distribution on the flow. Similarly, the normal force balance (2.8*b*) provides the so-called shape equation, written after simplification as

$$\begin{aligned} &k\Delta(H - \ell\sigma) + 2k(H - \ell\sigma)(2H^2 - K) - 2H\left[k_B T\sigma \left(\log\left(\frac{\sigma}{\sigma_s}\right) - 1 \right) + k(H - \ell\sigma)^2 \right] \\ &\quad - 2\nu[b^{\alpha\beta} d_{\alpha\beta} - w(4H^2 - 2K)] = p + 2\lambda H, \end{aligned} \tag{2.22}$$

where $\Delta(\cdot) = (\cdot)_{;\alpha\beta} a^{\alpha\beta}$ is the surface Laplacian. Equation (2.22) can be interpreted as the governing equation for the position field $\boldsymbol{r}$. Finally, the model is completed by the advection–diffusion equation for the protein density, which is written

$$\frac{\partial \sigma}{\partial t} + (v^{\alpha}\sigma)_{;\alpha} = D a^{\alpha\beta} \sigma_{,\alpha\beta} - \frac{2k\ell}{f} [a^{\alpha\beta}(H - \ell\sigma)_{,\alpha}\sigma_{,\beta} + \sigma a^{\alpha\beta}(H - \ell\sigma)_{,\alpha\beta}]. \tag{2.23}$$

The first term on the right-hand side captures Fickian diffusion of proteins, with diffusivity D (nm^2 $\cdot$ s^{-1}) given by the Stokes–Einstein relation: $D = k_B T/f$. The second term captures

the interaction of the curvature and protein gradients. The third term captures the effect of membrane shape on protein transport: mismatch between the mean curvature and the protein-induced spontaneous curvature serves as a source term for the transport of protein on the membrane surface.

2.7. *Comparison with other existing models*

The equations of motion (2.8) have appeared in the literature in many different forms. For example, the tangential stress balance (2.8*a*) is similar to (9) of Salbreux & Jülicher (2017) and (1) of Mietke, Julicher & Sbalzarini (2019). We eventually obtain (2.20) from this equation by using the constitutive relation (2.17) for the viscous stress, an equivalent expression of which can be found in (D11) of Torres-Sanchez *et al.* (2019). The final form of the tangential balance (2.20) also correlates to their equation (D9). Similarly, the normal force balance relation (2.8*b*) compares with (10) of Salbreux & Jülicher (2017) and (2) of Mietke *et al.* (2019). The final form of the force balance relations (2.20)–(2.22) captures the effect of curvature-inducing proteins that diffuse in the plane of the membrane. This differs from the model of Mietke *et al.* (2019) where the effect of protein-induced active tension was considered, or from the model of Salbreux & Jülicher (2017), which includes a contribution from the external stress and torque applied by the extracellular matrix. The advection–diffusion equation (2.23) in our model is also similar to (13) of Mietke *et al.* (2019), (3.27) of Mikucki & Zhou (2017), (2.12) of Nitschke, Voigt & Wensch (2012) and (4) of Gera & Salac (2017). These studies, however, did not include the strong coupling between bending and diffusion in (2.23), which results from the curvature inducing property of the membrane proteins. In the model presented by Mietke *et al.* (2019), the coupling between bending and diffusion occurs through an active tension induced by the proteins. Mikucki & Zhou (2017) calculated the phase field of protein density in an inviscid framework, Nitschke *et al.* (2012) solved the coupled in place flow and higher-order diffusion equation on a convective surface, while Gera & Salac (2017) solved a Cahn–Hilliard equation on a pre-existing curved surface.

3. Small deformations from the flat plane

3.1. *Linearization and dimensional analysis*

In this section, we specialize the governing equations presented in § 2.6 in a Monge parametrization assuming small deflections from the flat plane.

3.1.1. *Governing equations in the linear deformation regime*

The surface parametrization for a Monge patch is given by

$$\boldsymbol{r}(x, y, t) = x\boldsymbol{i} + y\boldsymbol{j} + z(x, y, t)\boldsymbol{k}, \tag{3.1}$$

where unit vectors $(\boldsymbol{i}, \boldsymbol{j}, \boldsymbol{k})$ form a fixed Cartesian orthonormal basis, and $z(x, y, t)$ is the deflection from the (x, y) plane. The tangent and normal vectors are given by

$$\boldsymbol{a}_1 = \boldsymbol{i} + z_{,x}\boldsymbol{k}, \quad \boldsymbol{a}_2 = \boldsymbol{j} + z_{,y}\boldsymbol{k}, \quad \boldsymbol{n} = \frac{1}{(1 + z_{,x}^2 + z_{,y}^2)^{1/2}}(-z_{,x}\boldsymbol{i} - z_{,y}\boldsymbol{j} + \boldsymbol{k}). \tag{3.2a–c}$$

The surface metric $(a_{\alpha\beta})$ and curvature metric $(b_{\alpha\beta})$ take the following forms

$$a_{\alpha\beta} = \begin{bmatrix} 1 + z_{,x}^2 & z_{,x}z_{,y} \\ z_{,y}z_{,x} & 1 + z_{,y}^2 \end{bmatrix}, \quad b_{\alpha\beta} = \frac{1}{(1 + z_{,x}^2 + z_{,y}^2)^{1/2}} \begin{bmatrix} z_{,xx} & z_{,xy} \\ z_{,yx} & z_{,yy} \end{bmatrix}. \tag{3.3a,b}$$

We further assume that deflections of the membrane from the flat configuration are small and simplify the governing equations in the limit of weak surface gradients $|\boldsymbol{\nabla} z| \ll 1$ by neglecting quadratic terms in $|\boldsymbol{\nabla} z|$ (Do 1976). In this limit, differential operators in the space of the membrane reduce to the Cartesian gradient, divergence and Laplacian in the (x, y) plane. The linearized governing equations for the intra-membrane flow become

$$\boldsymbol{\nabla} \cdot \boldsymbol{v} = 2wH, \tag{3.4}$$

$$\begin{aligned} &\boldsymbol{\nabla}\lambda + \nu\nabla^2\boldsymbol{v} + \nu\boldsymbol{\nabla}(\boldsymbol{\nabla}\cdot\boldsymbol{v}) - 4\nu w\boldsymbol{\nabla}H - 2\nu\boldsymbol{\nabla}w : \boldsymbol{\nabla}\boldsymbol{\nabla}z \\ &\quad = k\left(\nabla^2 z - 2\ell\sigma\right)\ell\boldsymbol{\nabla}\sigma - k_B T \log\left(\frac{\sigma}{\sigma_s}\right)\boldsymbol{\nabla}\sigma, \end{aligned} \tag{3.5}$$

whereas the shape equation expressing the normal momentum balance is

$$\begin{aligned} &k\left(\frac{1}{2}\nabla^4 z - \ell\nabla^2\sigma\right) - \nabla^2 z\left[k_B T\sigma\left(\log\left(\frac{\sigma}{\sigma_s}\right) - 1\right) + k\ell^2\sigma^2\right] \\ &\quad - \nu\left(\boldsymbol{\nabla}\boldsymbol{v} + \boldsymbol{\nabla}\boldsymbol{v}^{\mathrm{T}}\right) : \boldsymbol{\nabla}\boldsymbol{\nabla}z = p + \lambda\nabla^2 z. \end{aligned} \tag{3.6}$$

The transport equation for the protein density simplifies to

$$\frac{\partial\sigma}{\partial t} + \boldsymbol{\nabla}\cdot(\sigma\boldsymbol{v}) = D\nabla^2\sigma - \frac{k\ell}{f}\boldsymbol{\nabla}\left(\nabla^2 z - 2\ell\sigma\right)\cdot\boldsymbol{\nabla}\sigma - \frac{k\ell\sigma}{f}\left(\nabla^4 z - 2\ell\nabla^2\sigma\right). \tag{3.7}$$

We also note the linearized kinematic relation for the normal velocity

$$w = \frac{\partial z}{\partial t}. \tag{3.8}$$

3.1.2. *Non-dimensionalization*

We scale this system of equations using the following reference values. Length is non-dimensionalized by the size L of the domain, protein density by its reference value σ_0 and membrane tension by its far-field value λ_0. We also use the characteristic velocity scale $v_c = \lambda_0 L/\nu$ and time scale $t_c = L^2/D$. Denoting dimensionless variables with a tilde, the scaled governing equations are

$$\tilde{\boldsymbol{\nabla}}\cdot\tilde{\boldsymbol{v}} = 2\tilde{w}\tilde{H}, \tag{3.9}$$

$$\begin{aligned} &\tilde{\boldsymbol{\nabla}}\tilde{\lambda} + \tilde{\nabla}^2\tilde{\boldsymbol{v}} + \tilde{\boldsymbol{\nabla}}(\tilde{\boldsymbol{\nabla}}\cdot\tilde{\boldsymbol{v}}) - 4\tilde{w}\tilde{\boldsymbol{\nabla}}\tilde{H} - 2\tilde{\boldsymbol{\nabla}}\tilde{w} : \tilde{\boldsymbol{\nabla}}\tilde{\boldsymbol{\nabla}}\tilde{z} \\ &\quad = \tilde{\boldsymbol{\nabla}}\tilde{\sigma}\left[\frac{2\hat{C}\hat{B}}{\hat{T}}\tilde{\nabla}^2\tilde{z} - \frac{4\hat{C}^2\hat{B}^2}{\hat{T}}\tilde{\sigma} - \frac{2\hat{C}}{\hat{T}}\log\left(\frac{\tilde{\sigma}}{\tilde{\sigma}_s}\right)\right], \end{aligned} \tag{3.10}$$

$$\begin{aligned} &\tilde{\nabla}^4\tilde{z} - 2\hat{C}\hat{B}\tilde{\nabla}^2\tilde{\sigma} - \hat{C}\tilde{\nabla}^2\tilde{z}\left[2\tilde{\sigma}\left(\log\left(\frac{\tilde{\sigma}}{\tilde{\sigma}_s}\right) - 1\right) + 2\hat{C}\hat{B}^2\tilde{\sigma}^2\right] \\ &\quad - \hat{T}(\tilde{\boldsymbol{\nabla}}\tilde{\boldsymbol{v}} + \tilde{\boldsymbol{\nabla}}\tilde{\boldsymbol{v}}^{\mathrm{T}}) : \tilde{\boldsymbol{\nabla}}\tilde{\boldsymbol{\nabla}}\tilde{z} = \hat{P} + \hat{T}\tilde{\lambda}\tilde{\nabla}^2\tilde{z}, \end{aligned} \tag{3.11}$$

$$\begin{aligned} &\frac{\partial\tilde{\sigma}}{\partial\tilde{t}} + Pe\left(\tilde{\boldsymbol{v}}\cdot\tilde{\boldsymbol{\nabla}}\tilde{\sigma} + \tilde{\sigma}\tilde{\boldsymbol{\nabla}}\cdot\tilde{\boldsymbol{v}}\right) = \left(1 + 2\hat{C}\hat{B}^2\tilde{\sigma}\right)\tilde{\nabla}^2\tilde{\sigma} \\ &\quad + 2\hat{C}\hat{B}^2|\tilde{\boldsymbol{\nabla}}\tilde{\sigma}|^2 - \hat{B}\left(\tilde{\sigma}\tilde{\nabla}^4\tilde{z} + \tilde{\boldsymbol{\nabla}}\tilde{\nabla}^2\tilde{z}\cdot\tilde{\boldsymbol{\nabla}}\tilde{\sigma}\right). \end{aligned} \tag{3.12}$$

The expression for the normal velocity also becomes:

$$\tilde{w} = \frac{1}{Pe}\frac{\partial \tilde{z}}{\partial \tilde{t}}. \tag{3.13}$$

The dynamics is governed by five dimensionless parameters defined as follows. The ratio of the chemical potential to the bending rigidity of the membrane is denoted by $\hat{C} = L^2 k_B T \sigma_0/k$. The ratio of the length scale induced by the proteins and the membrane domain is given by $\hat{L} = \ell L \sigma_0$. The ratio of the intrinsic length scale of the membrane to the domain size is given by $\hat{T} = 2L^2\lambda_0/k$. The ratio between the bulk pressure and bending rigidity is denoted by $\hat{P} = 2L^3 p/k$. Finally, the Péclet number $Pe = \lambda_0 L^2/\nu D$ compares the advective transport rate to the diffusive transport rate. We define $\hat{B} = \hat{L}/\hat{C}$ for convenience of simulations and cast the equations in terms of $\hat{L}$, $\hat{B}$, $\hat{T}$ and Pe. Further, we assume that there is no pressure difference across the membrane ($\hat{P} = 0$).

3.2. *One-dimensional simulations*

We first explore the interplay between membrane bending and protein diffusion in the special case of a membrane that deforms as a string in one dimension, with a shape parameterized as $\tilde{z}(\tilde{x}, \tilde{t})$. The flow of lipids does not play a role in this scenario, and as a result in-plane velocity-dependent terms vanish in (3.9)–(3.12). The system of governing equations reduces to

$$\frac{\partial \tilde{\lambda}}{\partial \tilde{x}} = \frac{\partial \tilde{\sigma}}{\partial \tilde{x}}\left[\frac{2\hat{C}\hat{B}}{\hat{T}}\frac{\partial^2 \tilde{z}}{\partial \tilde{x}^2} - \frac{4\hat{C}^2\hat{B}^2}{\hat{T}}\tilde{\sigma} - \frac{2\hat{C}}{\hat{T}}\log\left(\frac{\tilde{\sigma}}{\tilde{\sigma}_s}\right)\right], \tag{3.14}$$

$$\frac{\partial \tilde{\sigma}}{\partial \tilde{t}} = (1 + 2\hat{C}\hat{B}^2\tilde{\sigma})\frac{\partial^2 \tilde{\sigma}}{\partial \tilde{x}^2} + 2\hat{C}\hat{B}^2\left(\frac{\partial \tilde{\sigma}}{\partial \tilde{x}}\right)^2 - \hat{B}\left[\tilde{\sigma}\frac{\partial^4 \tilde{z}}{\partial \tilde{x}^4} + \frac{\partial \tilde{\sigma}}{\partial \tilde{x}}\frac{\partial}{\partial \tilde{x}}\left(\frac{\partial^2 \tilde{z}}{\partial \tilde{x}^2}\right)\right], \tag{3.15}$$

$$\frac{\partial^4 \tilde{z}}{\partial \tilde{x}^4} - 2\hat{C}\hat{B}\frac{\partial^2 \tilde{\sigma}}{\partial \tilde{x}^2} - \hat{C}\frac{\partial^2 \tilde{z}}{\partial \tilde{x}^2}\left[2\tilde{\sigma}\left(\log\left(\frac{\tilde{\sigma}}{\tilde{\sigma}_s}\right) - 1\right) + 2\hat{C}\hat{B}^2\tilde{\sigma}^2\right] = \hat{P} + \hat{T}\tilde{\lambda}\frac{\partial^2 \tilde{z}}{\partial \tilde{x}^2}. \tag{3.16}$$

Equations (3.14)–(3.16) are solved numerically using a finite-difference scheme coded in Fortran 90 (numerical codes are available at https://github.com/armahapa/transport_phenomena_in_membranes). The tangential momentum balance (3.14), which can be viewed as an equation for the tension $\tilde{\lambda}$, is solved subject to the condition $\tilde{\lambda}(\tilde{x} = 0.5) = 1$, whereas the shape equation (3.16) is solved subject to clamped boundary conditions $\tilde{z} = 0$ and $\partial \tilde{z}/\partial \tilde{x} = 0$ at both ends of the domain $\tilde{x} = -0.5, 0.5$.

We first analysed the evolution of a symmetric patch of protein defined as $\tilde{\sigma}(\tilde{x}, \tilde{t} = 0) = 1/2[\tanh(20(\tilde{x} + 0.1)) - \tanh(20(\tilde{x} - 0.1))]$, subject to no-flux boundary conditions on $\tilde{\sigma}$ at the ends of the domain. Results from these simulations are shown in figure 1. In response to this protein distribution, the initial configuration of the membrane is bent (see figure 1(*a*) at $t = 0$). Over time, $\tilde{\sigma}$ homogenizes as a result of diffusion, and therefore the deflection $\tilde{z}$ decreases. At steady state, the distribution of protein is uniform on the membrane and $\tilde{z}$ is everywhere zero. The time evolution of $\tilde{z}$ at the centre of the string, corresponding to the maximum deflection, is shown in figure 1(*b*).

As a second example, we discuss the case where the protein density is initially zero and a time-dependent protein flux is prescribed at both boundaries as shown in figure 2(*a*). In response to the influx at the boundaries, the membrane deforms out of plane as the protein density increases; see figure 2(*b*). Once the flux returns to zero, diffusion homogenizes the

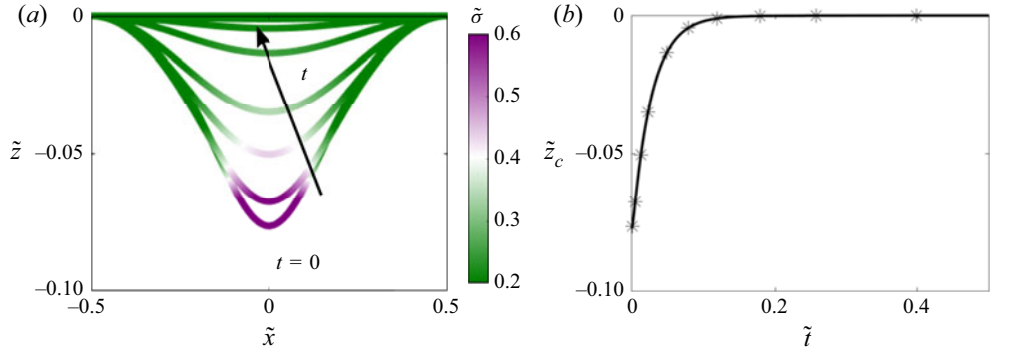

FIGURE 1. Protein density and membrane deformation in one dimension as functions of time, when an initial protein distribution and no-flux boundary conditions are prescribed. (*a*) Distribution of protein density plotted on the deformed one-dimensional membrane. (*b*) Time evolution of the maximum membrane deflection $\tilde{z}_c(\tilde{t}) = \tilde{z}(1/2, \tilde{t})$.

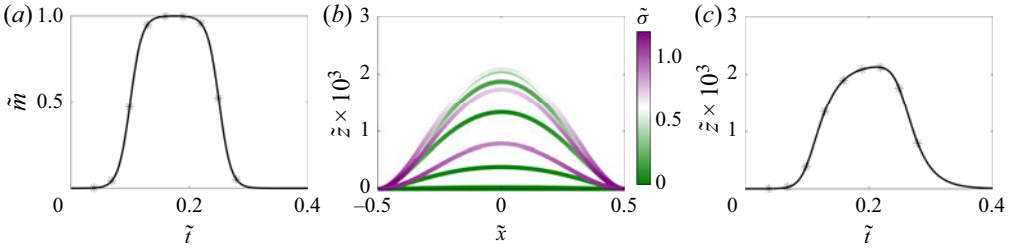

FIGURE 2. Evolution of membrane deformation and protein distribution when an influx of protein is prescribed at both boundaries. (*a*) Dimensionless boundary protein flux as a function of time. (*b*) Distribution of protein density plotted on the deformed membrane for $\hat{C} = 2.48 \times 10^{-1}$. Each shape corresponds to a specific time point. (*c*) Time evolution of the maximum membrane deflection $\tilde{z}_c$ for $\hat{C} = 2.48 \times 10^{-1}$. Symbols in panels (*a*,*c*) correspond to the time traces shown in (*b*).

protein, and the membrane height begins to decrease again. This effect is observed clearly by looking at the deformation at the centre of the string as a function of time in figure 2(*c*), which closely follows the dynamics of the boundary flux shown in figure 2(*a*).

In both examples of figures 1 and 2, we note that the protein distribution becomes uniform at long times (in the absence of any boundary flux), and as a result the membrane returns to its flat reference shape. At first glance, this result seems counter-intuitive since there is a non-zero density of curvature-inducing proteins on the membrane. But as Chabanon and Rangamani showed previously, for a uniform distribution of proteins with no-flux boundary conditions on the membranes, minimal surfaces are admissible solutions for the membrane geometry (Chabanon & Rangamani 2018, 2019). In the case of closed geometries on vesicle, constant mean curvature surfaces are admissible solutions (Zhong-Can & Helfrich 1989; Seifert 1993; Góźdź & Gompper 1998; Campelo & Hernández-Machado 2007). In the case of interest here, a flat membrane is the admissible solution for the boundary conditions associated with $\tilde{z}$, and a proof of this result is given in appendix A.

3.3. *Two-dimensional simulations*

3.3.1. *Numerical implementation*

We solved the set of governing equations (3.9)–(3.12) in two dimensions inside a square domain using a finite-difference technique that we outline here. Our numerical scheme is second order in space and first order in time. We note that time only appears explicitly in the advection–diffusion equation (3.12) for the protein density: we solve it using a semi-implicit scheme wherein the linear diffusion term is treated implicitly while the nonlinear advective terms and curvature-induced transport terms are treated explicitly. The remaining governing equations are all elliptic in nature and can be recast as a series of Poisson problems as we explain. First, we note that the shape equation (3.11) is biharmonic and can thus be recast into two nested Poisson problems providing the shape $\tilde{z}$ at a particular time step. To solve for the surface tension $\tilde{\lambda}$, we take the divergence of the tangential momentum balance (3.10) and combine it with the continuity equation (3.9) to obtain the Poisson equation

$$\tilde{\nabla}^2\tilde{\lambda} + f = 0, \tag{3.17}$$

where

$$\begin{aligned} f = {} & 4\tilde{H}\tilde{\nabla}^2\tilde{w} - 2\tilde{\boldsymbol{\nabla}}\tilde{\boldsymbol{\nabla}}\tilde{z} : \tilde{\boldsymbol{\nabla}}\tilde{\boldsymbol{\nabla}}\tilde{w} \\ & - \frac{2\hat{C}\hat{B}}{\hat{T}}\tilde{\boldsymbol{\nabla}}\tilde{\nabla}^2\tilde{z}\cdot\tilde{\boldsymbol{\nabla}}\tilde{\sigma} - \left[\frac{2\hat{C}\hat{B}}{\hat{T}}\tilde{\nabla}^2\tilde{z} - \frac{2\hat{C}}{\hat{T}}\log\left(\frac{\tilde{\sigma}}{\tilde{\sigma}_s}\right)\right]\tilde{\nabla}^2\tilde{\sigma} \\ & + \frac{2\hat{C}}{\hat{T}}\tilde{\boldsymbol{\nabla}}(\log\tilde{\sigma})\cdot\tilde{\boldsymbol{\nabla}}\tilde{\sigma} + \frac{2\hat{C}^2\hat{B}^2}{\hat{T}}\tilde{\nabla}^2\tilde{\sigma}^2. \end{aligned} \tag{3.18}$$

Note that there is no natural boundary condition on $\tilde{\lambda}$ at the edges of the domain. To approximate an infinite membrane, we first estimate the tension along the four edges using the integral representation

$$\tilde{\lambda}(\tilde{\boldsymbol{r}}) = 1 + \int_{\Omega} G(\tilde{\boldsymbol{r}} - \tilde{\boldsymbol{r}}_0) f(\tilde{\boldsymbol{r}}_0)\,\mathrm{d}A(\tilde{\boldsymbol{r}}_0), \tag{3.19}$$

where $G(\boldsymbol{r}) = -\log r/2\pi$ is the two-dimensional (2-D) Green's function for Poisson's equation in an infinite domain. The calculated tension along the edges is then used as the boundary condition for (3.17), where the normal velocity component at the current time step k is calculated as

$$\tilde{w}^k = \frac{1}{Pe}\frac{\tilde{z}^k - \tilde{z}^{k-1}}{\Delta\tilde{t}}. \tag{3.20}$$

With knowledge of the membrane tension, the tangential momentum balance (3.10) then provides two modified Poisson problems for the in-plane velocity components. Note that the equations for $\tilde{z}$, $\tilde{\lambda}$ and $\tilde{\boldsymbol{v}}$ are nonlinearly coupled through the various forcing terms in their respective Poisson problems. To remedy this problem, we iterate their solution until every variable converges with a tolerance limit of 5×10^{-7} before proceeding to the next time step. All the results presented below were obtained on a spatial uniform grid of size 201×201 and with a dimensionless time step of $\Delta\tilde{t} = 10^{-4}$. We used Fortran 90 for compiling and running the algorithm. As we show in appendix B, the numerical method was successfully validated by comparison with a Stokes–Neumann formulation (Glowinski *et al.* 2005).

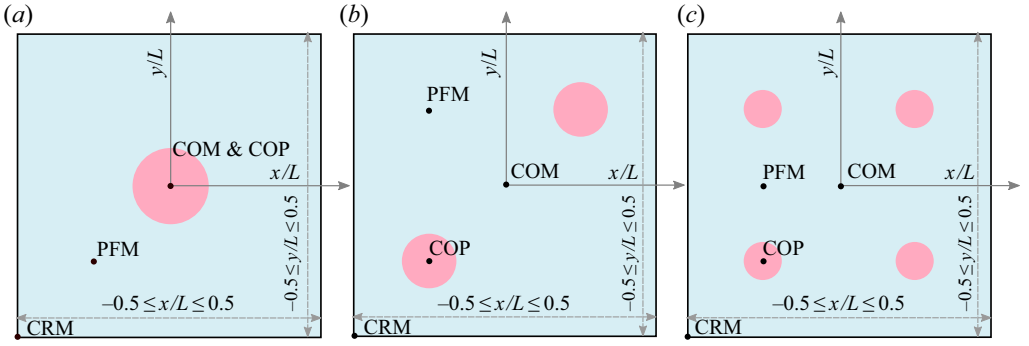

FIGURE 3. System set-up and initial condition used in 2-D simulations. All 2-D simulations are performed for a linearized Monge patch. We simulate the dynamics for three different initial distributions of proteins as shown. The total area fraction of protein is same for the three cases, with proteins covering 10 % of the total area. (*a*) Single patch of protein placed at the centre $(0, 0)$. (*b*) Two patches of protein placed at diametrically opposite positions with centre locations $(-0.25, -0.25)$ and $(0.25, 0.25)$. (*c*) Four patches of proteins placed at four diagonal positions: $(-0.25, -0.25)$, $(-0.25, 0.25)$, $(0.25, -0.25)$ and $(0.25, 0.25)$. The following abbreviations are used in subsequent figures to track the system behaviour: COM: centre of the membrane, COP: centre of the patch, CRM: corner of the membrane and PFM: protein-free membrane.

3.3.2. *Two-dimensional simulation results*

Using the numerical scheme described above, we solved the linearized two-dimensional governing equations (3.9)–(3.12) for different initial conditions. In all cases, the boundary conditions for the membrane shape were set to $\tilde{z} = 0$ and $\boldsymbol{\nu} \cdot \nabla \tilde{z} = 0$ where $\boldsymbol{\nu}$ is the in-plane normal to the edge of the domain, and no-flux boundary conditions were enforced on the protein distribution. We considered three different initial conditions for the protein density as depicted in figure 3, namely: a single circular patch at the centre of the domain (figure 3*a*), two identical patches placed at diametrically opposite ends of the domain (figure 3*b*) and four patches centred in each quadrant of the domain (figure 3*c*). The total mass of protein is the same in all three cases, only the initial spatial distribution is different. For the velocity and tension, we maintain open boundary conditions as noted in § 3.3.1.

We tracked the dynamics of the membrane shape, protein distribution, membrane tension and velocity for a single patch of proteins corresponding to figure 3(*a*) in figure 4. The initial membrane configuration is bent to accommodate the initial distribution of proteins (figure 4*a*), and the membrane tension for this initial distribution is heterogeneous as seen in figure 4(*d*), consistent with our previous results (Rangamani *et al.* 2014; Hassinger *et al.* 2017). Over time, the proteins diffuse from the centre of the patch across the membrane, tending towards a homogeneous distribution (figure 4*b*,*c*), and this process is accompanied by a reduction in the membrane deflection. The homogenization of proteins results in homogenization of the membrane tension, which approaches its value at infinity (figure 4*e*,*f*). The tangential velocity is directed outward (figure 4*g*–*i*), and the dimensionless magnitude of the maximum velocity in figure 4(*g*) is 4.8×10^{-3}. Expectedly, the magnitude of this velocity decreases with time as seen in figure 4(*h*,*i*).

When the proteins are distributed in two and four patches as shown in figure 3(*b*,*c*), we found that the overall behaviour of the system was quite similar to a single patch with some changes to the dynamics. First, because each patch had a lower density of proteins (half or quarter), the initial deformation was smaller and the protein distribution homogenized faster than in the case of a single patch (figure 5*a*,*b*). Similarly, the typical magnitude of

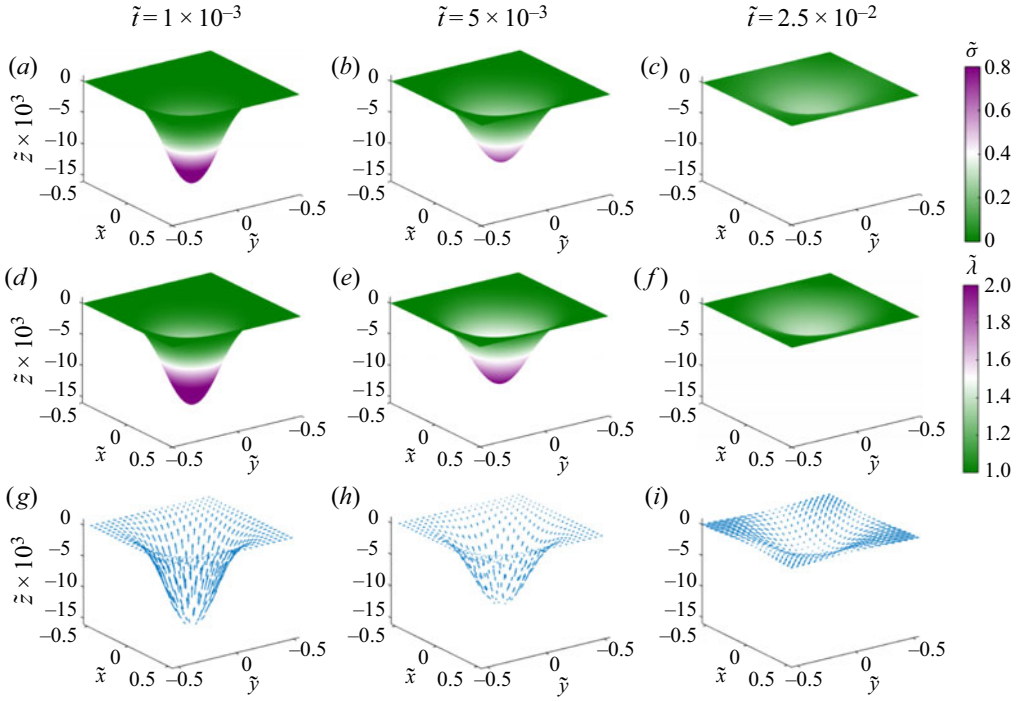

FIGURE 4. Dynamics of the evolution of membrane shape, protein distribution, membrane tension and tangential velocity field for a single patch of protein at three different times. (*a–c*) Distributions of membrane protein density are shown at dimensionless times 1×10^{-3}, 5×10^{-3} and 2.5×10^{-2}. (*d*,*e*) Distributions of membrane tension at the same non-dimensional times. (*g–i*) Tangential velocity fields shown at the same non-dimensional times. Arrows are scaled according to tangential velocity magnitude, with a maximum dimensionless velocity of 4.3×10^{-3}.

membrane tension variations (figure 5*c*,*d*) and of the tangential velocity field (figure 5*e*,*f*) was also smaller to begin with and the system attained the homogeneous distribution rapidly.

To compare the effects of one, two and four patches directly, we plotted the membrane deformation (figure 6), membrane protein distribution (figure 7) and membrane tension distribution (figure 8) at different locations for each case. The initial deformation is different for the different cases because of the differences in the local density of proteins. For a single patch, we observed that the maximum deformation occurs at the centre of the patch and it takes a longer time for this deformation to go to zero in the case of a single patch compared to multiple patches (compare figure 6*a* to 6*b*,*c*). In the case of two and four patches, we also observe a small positive deformation at the centre of the membrane and in the protein-free membrane. This can be explained by the fact that the continuity conditions of the surface will result in a small but upward displacement in protein-free regions in response to the large downward displacement in the regions where the proteins are initially present.

Comparing the protein dynamics for one, two and four patches, we observed that increasing the number of patches decreases the time it takes for the protein distribution to homogenize across the membrane domain (figure 7). Thus, although membrane bending

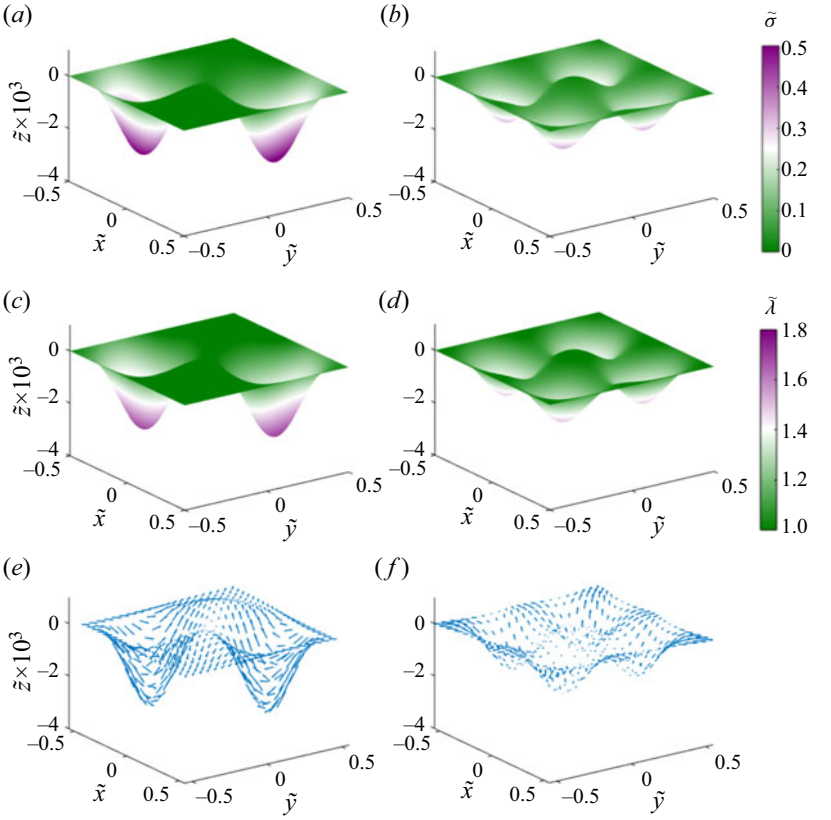

FIGURE 5. Dynamics of the evolution of membrane shape, protein distribution, membrane tension and tangential velocity field for two and four patches of protein at dimensionless time $\tilde{t} = 5 \times 10^{-3}$. The left column shows the distribution of protein density (*a*), membrane tension (*c*) and tangential velocity (*e*) for two patches of protein. The right column shows the distribution of protein density (*b*), membrane tension (*d*) and tangential velocity (*f*) for four patches of protein. The magnitude of the maximum dimensionless tangential velocity is 1.6×10^{-2} in the case of two patches, and 4.1×10^{-3} in the case of four patches.

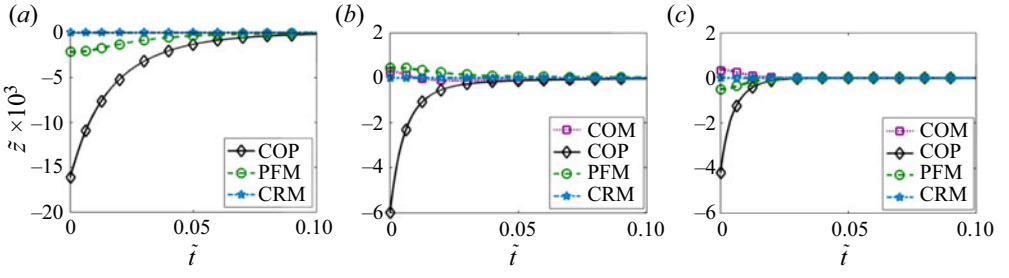

FIGURE 6. Temporal evolution of the membrane deflection at the various locations defined in figure 3 for a single patch of protein (*a*), two patches (*b*) and four patches (*c*).

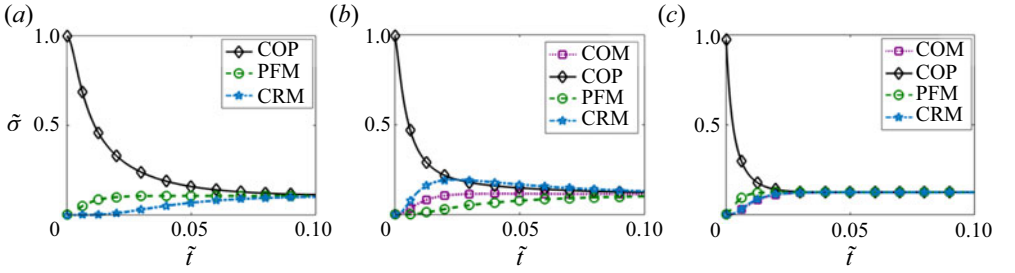

FIGURE 7. Temporal evolution of the protein density at the locations defined in figure 3 for a single patch of protein (*a*), two patches (*b*) and four patches (*c*).

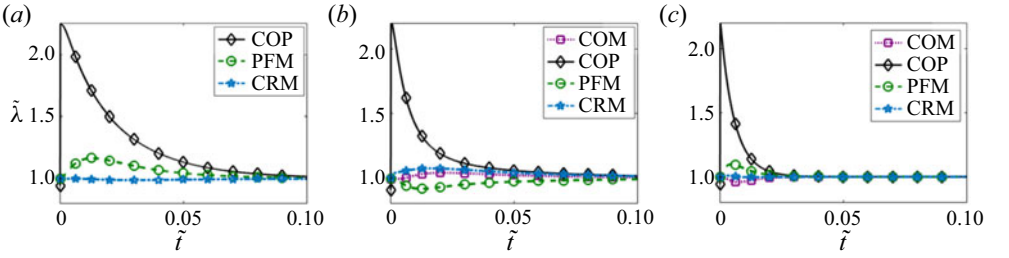

FIGURE 8. Temporal evolution of the membrane tension at the locations defined in figure 3 for a single patch of protein (*a*), two patches (*b*) and four patches (*c*).

and protein distribution are coupled, the distribution of multiple patches weakens the coupling and promotes rapid homogenization of the membrane proteins. While the steady state protein distribution is the same in all cases, the dynamics with which the protein-free regions show an appreciable increase in proteins also depends on the initial distribution of proteins. For example, in the case of a single patch, CRM takes much longer to reach steady state compared to the case of two or four patches. Figure 7 shows that for the initial conditions of a single patch and of four patches of protein, $\tilde{\sigma}$ approaches the uniform protein density monotonically. But for the case of two patches, the time evolution of the protein density is not monotonic, and we found the density of protein at the corner of the membrane exceeds the density at the COP for a brief time interval. We investigated this phenomenon further and studied the dependence on intra-membrane flow by varying the Péclet number in § 3.3.3.

Similar dynamics is observed for the membrane tension as well. Figure 8 shows that the membrane tension takes a larger time to reach its steady value for the case of one or two patches when compared to four patches (compare figure 8*a–c*). The initial rise in the membrane tension corresponds to the inviscid response of the membrane to the curvature-inducing protein distribution, while from the next time step onwards tension changes primarily due to viscous effects.

3.3.3. *Effect of fluid advection on coupled membrane–protein dynamics*

Next, we investigated the effect of fluid advection in the case of two patches by varying the Péclet number *Pe* in figure 9. We observed that at the centre of the patch (figure 9*a*) there was no observable effect on the temporal evolution of the protein density. However, at the centre of the membrane (figure 9*b*) and in the protein-free membrane (figure 9*c*),

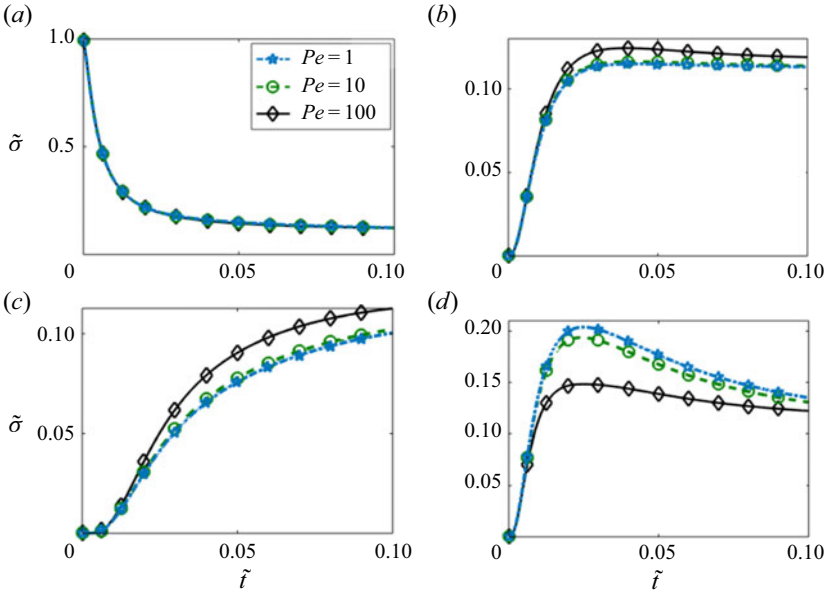

FIGURE 9. Temporal evolution of local protein density for different values of the Péclet number in the case of two patches of protein. The protein density is measured at the four locations defined in figure 3: COM (*a*), COP (*b*), PFM (*c*) and CRM (*d*).

we observed that increasing Péclet number had a small effect on the dynamics of the protein density, particularly at long times.

The effect of increasing the Péclet number was most dramatic at the corner of the membrane (figure 9*d*), where the initial rise in the protein density was found to be similar for all three values of *Pe*, but the increase resulted in a higher value for lower *Pe*. Eventually, $\tilde{\sigma}$ at the corner decreases towards the mean value of $\tilde{\sigma}$ over time. Thus, the coupling between lipid flow and protein diffusion seems to have a larger impact on transport in the regions that are initially protein free.

To further investigate the role of convective transport, we tracked the separation distance $\tilde{l}_{sep}$ between the centres of mass of two effective patches (l_{sep}) as a function of time in figure 10. The centre of mass of a patch is formally defined as

$$\tilde{\boldsymbol{r}}_c = \frac{\displaystyle\int_\Omega \tilde{\boldsymbol{r}}(\tilde{\sigma} - \tilde{\sigma}_m)\mathcal{H}(\tilde{\sigma} - \tilde{\sigma}_m)\,\mathrm{d}a}{\displaystyle\int_\Omega (\tilde{\sigma} - \tilde{\sigma}_m)\mathcal{H}(\tilde{\sigma} - \tilde{\sigma}_m)\,\mathrm{d}a} \quad \text{with, } \tilde{\sigma}_m = \int_\Omega \tilde{\sigma}\,\mathrm{d}a, \tag{3.21}$$

where the effective extent of the patch is defined using the Heaviside function $\mathcal{H}$ as the area where protein density exceeds its mean value. We observed that $\tilde{l}_{sep}$ increases with time and decreases with increasing Péclet number (figure 10). This can be explained from the velocity profile for two patches in figure 5(*e*). The direction of the velocity is towards the centre of the membrane in the area where the patch is located. Therefore, the advective transport due to the lipid tends to weaken the separation otherwise caused by diffusion. Since the effect of flow increases with increasing *Pe*, the separation of the two patches slows down for higher values Péclet number as shown in figure 10. This also explains the

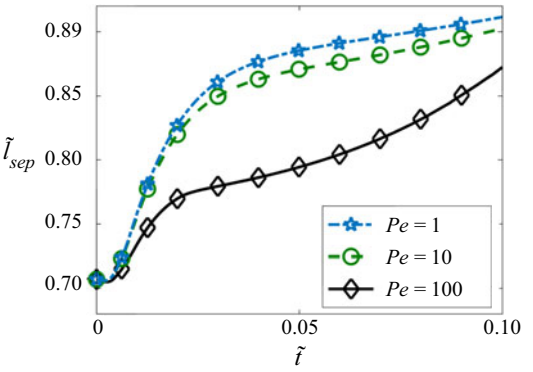

FIGURE 10. Evolution of the separation distance between the centroids of the protein patches in the case of two patches and for three different values of the Péclet number.

decrease of density of the protein at the CRM and the increase of the protein density at the PFM and COM with higher value of *Pe* as found in figure 9.

We can further understand the dynamics of the separation distance between the two patches by considering the diffusion of a protein patch in one triangular half-domain of lipid. This triangle is bounded by two of the domain boundaries and by the diagonal of the square domain that passes in between the two patches. The diagonal line is also a line of symmetry, and thus behaves as an effective no-flux boundary for the triangular half of the domain. Therefore, each triangular half-domain is subject to the no-flux condition on its three sides. In this half-domain, the semicircular half-patch of protein facing the corner of the membrane diffuses to a smaller area compared to the other semicircle that faces the centre of the membrane. This results in an effectively larger protein gradient towards CRM. Therefore, the protein density shifts towards the protein-free corner and results in an effective shift of the patches towards the corners of the membrane.

4. Axisymmetric membranes

In the previous section, we focused on small deformations from a flat plane. However, membranes are known to undergo large deformations including bud-like shapes in the presence of proteins (Dannhauser & Ungewickell 2012; Hassinger *et al.* 2017; Haucke & Kozlov 2018). Here, we illustrate the interaction between membrane bending and protein diffusion for membrane buds. For these simulations, we assume that the membrane is rotationally symmetric and recast the governing equations of § 2.6 in an axisymmetric framework.

4.1. *Governing equations in axisymmetric coordinates*

We represent tangential velocity vector in polar coordinates as

$$\boldsymbol{v} = v^s \boldsymbol{e}_s + v^\theta \boldsymbol{e}_\theta. \tag{4.1}$$

For an axisymmetric geometry as depicted in figure 11(*a*), we assume $\partial()/\partial\theta = 0$ and $v^\theta = 0$ (Arroyo & DeSimone 2009). Thus, we parametrize the geometry as

$$\boldsymbol{r}(s, \theta, t) = r(s, t)\boldsymbol{e}_r + z(s, t)\boldsymbol{k}, \tag{4.2}$$

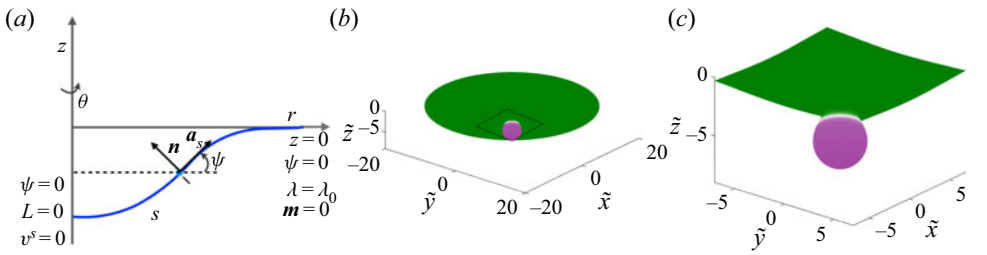

FIGURE 11. Parametrization of an axisymmetric membrane and bud-shaped initial condition. (*a*) Parametrization and boundary conditions for an axisymmetric membrane. (*b*) Solution domain showing the initial condition, where a circular patch of curvature-inducing protein (shown in purple) induces a bud-shaped deformation. (*c*) A magnified view of the domain shown in (*a*).

where the unit vectors $(\boldsymbol{e}_r, \boldsymbol{e}_\theta, \boldsymbol{k})$ are a set of orthonormal basis vectors and s is the arclength measured from the axis of symmetry. The tangent and normal vectors are given by

$$\boldsymbol{a}_s = \cos\psi \boldsymbol{e}_r + \sin\psi \boldsymbol{e}_\theta, \quad \boldsymbol{a}_\theta = r\boldsymbol{e}_\theta, \quad \boldsymbol{n} = -\sin\psi \boldsymbol{e}_r + \cos\psi \boldsymbol{e}_\theta, \tag{4.3a–c}$$

where ψ is the angle made by the tangent $\boldsymbol{a}_s$ with the radial unit vector $\boldsymbol{e}_r$. The corresponding surface metric $(a_{\alpha\beta})$ and curvature metric $(b_{\alpha\beta})$ are

$$a_{\alpha\beta} = \begin{bmatrix} 1 & 0 \\ 0 & r^2 \end{bmatrix}, \quad b_{\alpha\beta} = \begin{bmatrix} \psi_{,s} & 0 \\ 0 & r\sin\psi \end{bmatrix}. \tag{4.4a,b}$$

Using these expressions, the incompressibility constraint becomes

$$\frac{1}{r}\frac{\partial (r v^s)}{\partial s} = 2wH. \tag{4.5}$$

The governing equation for surface pressure is

$$\begin{aligned} &\frac{\partial \lambda}{\partial s} - 4\nu w \frac{\partial H}{\partial s} + 2\nu\left(2\frac{\partial wH}{\partial s} + K v_s - \frac{\partial w}{\partial s}\frac{\partial \psi}{\partial s}\right) \\ &\quad = -\frac{\partial \sigma}{\partial s}\left[k_B T \log\left(\frac{\sigma}{\sigma_s}\right) - 2k\ell(H - \ell\sigma)\right], \end{aligned} \tag{4.6}$$

and the shape equation expressing the normal momentum balance is given by

$$\begin{aligned} &k\frac{1}{r}\frac{\partial}{\partial s}\left(r\frac{\partial (H-\ell\sigma)}{\partial s}\right) + 2k(H-\ell\sigma)(2H^2 - K) \\ &\quad - 2H\left[k_B T\sigma\left(\log\left(\frac{\sigma}{\sigma_s}\right) - 1\right) + k(H-\ell\sigma)^2\right] \\ &\quad - 2\nu\left[\frac{\partial \psi}{\partial s}\frac{\partial v^s}{\partial s} + \frac{\sin\psi\cos\psi v^s}{r^2} - w(4H^2 - 2K)\right] = p + 2\lambda H. \end{aligned} \tag{4.7}$$

The transport equation for the protein density simplifies to

$$\frac{\partial \sigma}{\partial t}+\frac{\partial(\sigma v^s)}{\partial s}=D\frac{1}{r}\frac{\partial}{\partial s}\left(r\frac{\partial \sigma}{\partial s}\right)-2k\ell\left[\sigma\frac{1}{r}\frac{\partial}{\partial s}\left(r\frac{\partial H}{\partial s}\right)+\left(\frac{\partial H}{\partial s}\right)^2\right]$$
$$+2k\ell^2\left[\sigma\frac{1}{r}\frac{\partial}{\partial s}\left(r\frac{\partial \sigma}{\partial s}\right)+\left(\frac{\partial \sigma}{\partial s}\right)^2\right]. \tag{4.8}$$

Finally, the kinematic relation for the normal velocity is given by

$$w=\boldsymbol{n}\cdot\frac{\partial \boldsymbol{r}}{\partial t}. \tag{4.9}$$

4.2. *Non-dimensionalization*

We non-dimensionalize the system of equations using a reference length scale L (which we assumed to be 20 nm) such that the radius of the domain is $20L$, with all other scales remaining the same as in § 3.1.2. The dimensionless governing equations are

$$\frac{1}{\tilde r}\frac{\partial(\tilde r\tilde v^s)}{\partial \tilde s}=2\tilde w\tilde H, \tag{4.10}$$

$$\frac{\partial \tilde\lambda}{\partial \tilde s}-4\tilde w\frac{\partial \tilde H}{\partial \tilde s}+2\left(2\frac{\partial \tilde w\tilde H}{\partial \tilde s}+K\tilde v_s-\frac{\partial \tilde w}{\partial \tilde s}\frac{\partial \psi}{\partial \tilde s}\right)$$
$$=-\frac{\partial \tilde\sigma}{\partial \tilde s}\left[\frac{2\hat C}{\hat T}\log\left(\frac{\tilde\sigma}{\tilde\sigma_s}\right)-\frac{4\hat C\hat B}{\hat T}(\tilde H-\hat C\hat B\tilde\sigma)\right], \tag{4.11}$$

$$\frac{1}{\tilde r}\frac{\partial}{\partial \tilde s}\left(\tilde r\frac{\partial(\tilde H-\hat C\hat B\tilde\sigma)}{\partial \tilde s}\right)+2(\tilde H-\hat C\hat B\tilde\sigma)(2\tilde H^2-K)$$
$$-2\tilde H\left[\hat C\tilde\sigma\left(\log\left(\frac{\tilde\sigma}{\tilde\sigma_s}\right)-1\right)+(\tilde H-\hat C\hat B\tilde\sigma)^2\right]$$
$$-\hat T\left[\frac{\partial \psi}{\partial \tilde s}\frac{\partial v^s}{\partial \tilde s}+\frac{\sin\psi\cos\psi\,\tilde v^s}{\tilde r^2}-\tilde w(4\tilde H^2-2\tilde K)\right]=\frac{\hat P}{2}+\hat T\tilde\lambda\tilde H, \tag{4.12}$$

$$\frac{\partial \tilde\sigma}{\partial \tilde t}+Pe\frac{\partial(v^\alpha\tilde\sigma)}{\partial \tilde s}=\frac{1}{\tilde r}\frac{\partial}{\partial \tilde s}\left(\tilde r\frac{\partial \tilde\sigma}{\partial \tilde s}\right)$$
$$-2\hat B\left[\frac{\partial(\tilde H-\hat C\hat B\tilde\sigma)}{\partial \tilde s}\frac{\partial \tilde\sigma}{\partial \tilde s}+\tilde\sigma\frac{1}{\tilde r}\frac{\partial}{\partial \tilde s}\left(\tilde r\frac{\partial(\tilde H-\hat C\hat B\tilde\sigma)}{\partial \tilde s}\right)\right], \tag{4.13}$$

$$\tilde w=\frac{1}{Pe}\boldsymbol{n}\cdot\frac{\partial \tilde{\boldsymbol{r}}}{\partial \tilde t}. \tag{4.14}$$

4.3. *Numerical implementation*

The system of dimensionless governing equations (4.11)–(4.14) was solved using finite-difference methods using the arclength parametrization (Rangamani, Behzadan & Holst 2020). In these simulations, the total area of the domain was kept constant. This was achieved by first dividing the initial arclength into $N-1$ discrete elements, which gives N grid points on which the equations were solved. We then calculated the area of each of the $N-1$ discrete area elements. At each time step, the local radius and arclength is back calculated by keeping the area of these discrete elements constant in the following way:

$$r_{i+1}^2 = r_i^2 + 2\,\mathrm{d}A_i \cos\psi/\pi, \tag{4.15}$$

and

$$s_{i+1} = s_i + \mathrm{d}s_i = s_i + \frac{r_{i+1} - r_i}{\cos\psi}, \tag{4.16}$$

with

$$r_1 = s_1 = 0. \tag{4.17}$$

To solve the set of governing equations (4.11)–(4.14), we first obtained the membrane tension $\tilde{\lambda}$ by integrating (4.11) backward starting from the edge of the membrane where the boundary condition $\tilde{\lambda} = 1$ is enforced. We then consider the shape equation (4.12) where the first term can be written as $(1/\tilde{r})(\partial\tilde{L}/\partial\tilde{s})$ in terms of the normal bending stress (Steigmann *et al.* 2003)

$$\frac{\tilde{L}}{\tilde{r}} = \frac{\partial}{\partial\tilde{s}}\left[\frac{1}{2}\left(\psi_s + \frac{\sin\psi}{\tilde{r}}\right) - \hat{C}\hat{B}\tilde{\sigma}\right]. \tag{4.18}$$

The modified shape equation is solved for $\tilde{L}$ with boundary condition $\tilde{L} = 0$ at the centre of the domain corresponding to the case where there is no pulling force acting on the centre of the membrane. When doing do, other shape-dependent terms in the shape equation are treated explicitly, and iterations are performed until convergence. Equation (4.18) is then integrated for ψ at every point with the boundary condition $\psi = 0$ at the centre of the membrane and at the boundary. Having determined ψ, the radial $\tilde{r}$ and the vertical $\tilde{z}$ position of the membrane are calculated. The continuity equation (4.10) is then integrated to obtain the value of tangential velocity $\tilde{v}^s$. Finally, the diffusion equation (4.13) is marched in time to update the protein distribution $\tilde{\sigma}$ across the membrane as described in § 3.3.1.

4.4. *Numerical results*

We solved the dimensionless governing equations (4.10)–(4.14) for the solution domain and boundary conditions shown in figure 11(*a*). The domain is initialized with a protein distribution as shown in figure 11(*b*) such that the initial shape of the membrane is a bud, similar to those observed in membrane fission and fusion processes (Jahn, Lang & Südhof 2003; Kozlovsky & Kozlov 2003). This initial shape is obtained by solving (4.5)–(4.9) for an inviscid membrane. The black square highlights the curved bud region shown as a zoomed-in image in figure 11(*c*), and all simulation results are shown in this zoomed-in region.

We make no simplifying assumptions about linear deformations or curvature regimes in the axisymmetric case, which allows us to explore the nonlinear coupling between membrane curvature, protein diffusion, and lipid flow in full detail. We conducted the

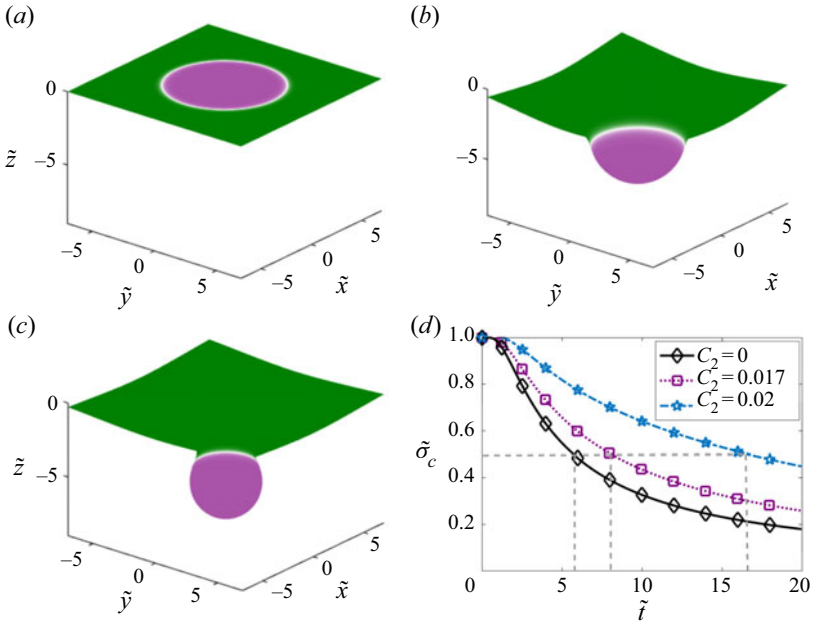

FIGURE 12. Dependence of surface curvature C_2 on the diffusion of the protein that does not induce curvature ($\ell_1 = 0$). Initial protein distribution on: (*a*) a flat membrane ($C_2 = 0$), (*b*) a membrane with pre-existing curvature $C_2 = 0.017$ nm^{-1}, (*c*) a membrane with pre-existing curvature $C_2 = 0.02$ nm^{-1}. (*d*) Temporal dynamics of protein density at the centre of the membrane for the three different configurations. The dashed lines highlight the time it takes for $\tilde{\sigma}_c$ to decrease from 1 to 0.5.

following simulations to map this relationship: (a) diffusion of proteins on curved surfaces with no coupling between protein distribution and spontaneous curvature, so as to study the effect of surface curvature on protein diffusion, and (b) coupled diffusion of proteins and induction of spontaneous curvature.

We first investigate the diffusion of proteins on curved surfaces by simulating the scenario where there are two types of proteins on the membrane: the first protein does not induce any curvature ($C_1 = 0$) but can diffuse along the membrane ($D_1 = 0.1$ μm^2 s^{-1}), whereas the second protein is curvature inducing (with spontaneous curvature $C_2 = 0.02$ nm^{-1}) but immobile ($D_2 = 0$). Figure 12(*a–c*) shows the initial shapes of the three surfaces for increasing values of the spontaneous curvature. Figure 12(*a*) shows the case of a flat membrane ($C_2 = 0$) and captures diffusion of a protein with no spontaneous curvature ($\ell = 0$) similar to Fickian diffusion on a flat plane. When the membrane is moderately curved in figure 12(*b*) or heavily curved in figure 12(*c*), diffusion from the centre of the membrane takes a longer time compared to Fickian diffusion on a flat plane (compare purple and blue lines with the black line in figure 12*d*). The time required for proteins to diffuse away from the centre to the flat regions of the membrane increases with the pre-existing curvature. We compared the time taken for $\tilde{\sigma}_c$ to decrease from 1 to 0.5 and find that it increases nonlinearly with C_2, as shown by the dashed lines in figure 12(*d*). This result clearly shows that the curvature of the surface alters the timescale of surface diffusion in a nonlinear fashion.

Next, we simulated the full coupled system where the same protein induces spontaneous curvature and is free to diffuse in the plane of the membrane. Figure 13 tracks the

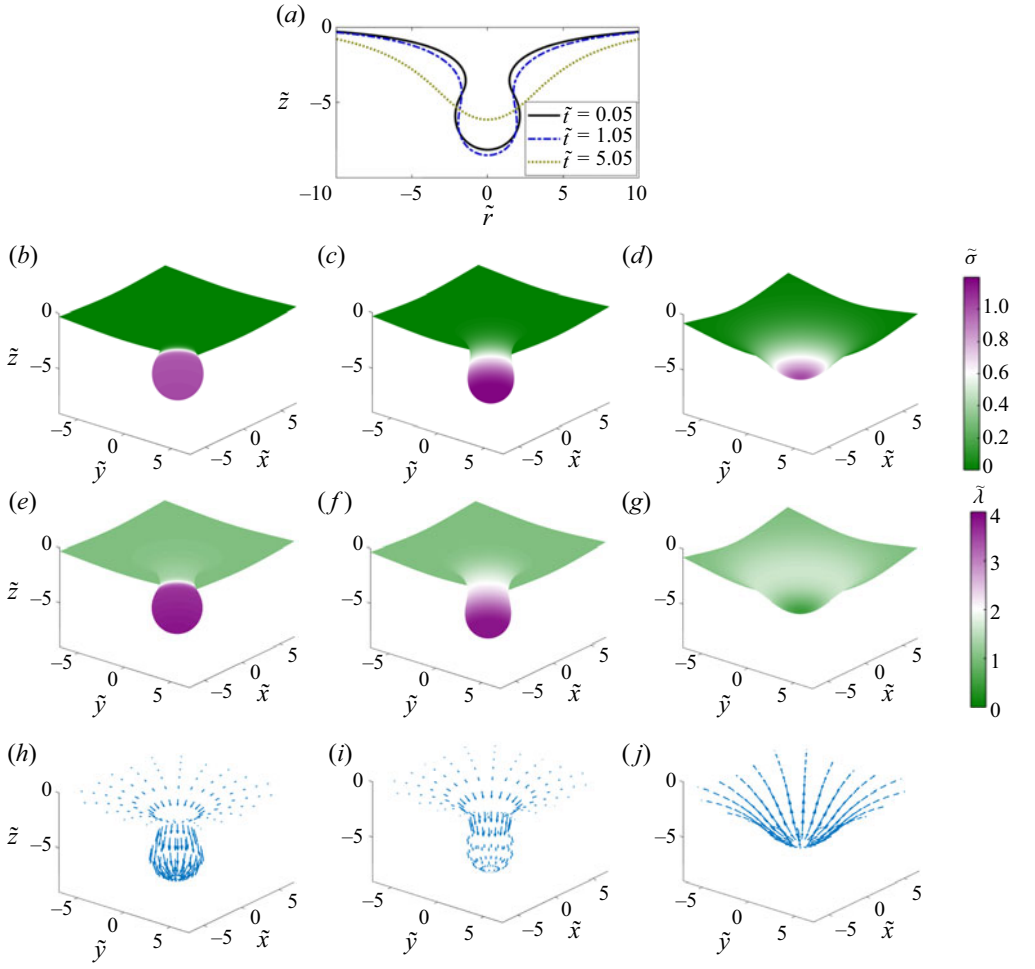

FIGURE 13. Dynamics of the evolution of membrane shape, protein distribution, membrane tension and tangential velocity field at three different times. (*a*) Superposed membrane shapes at three different times. (*b–d*) Distributions of membrane protein density are shown at dimensionless times 0.05, 1.05 and 5.05. (*e–g*) Distributions of membrane tension at the same non-dimensional times. (*h–j*) Tangential velocity fields shown at the same non-dimensional times. Arrows are scaled according to tangential velocity magnitude, with a maximum dimensionless velocity of 8.4×10^{-2}.

evolution of the membrane shape and protein distribution as the initial aggregate of curvature-inducing protein diffuses over time. At the start of the simulation, the membrane forms an Ω-shaped bud with a narrow neck (figure 13*b*). The equilibrium solution of this system is a flat plane with uniform protein distribution. Upon initiation of the simulation, the membrane neck widens and forms a U-shaped neck. This widening of the neck is accompanied by a brief increase in the height of the tip of the membrane and a brief accumulation of proteins towards the bud (figure 13*b*,*c*). Once the U-shaped neck is formed, the direction of transport reverses and proteins diffuse rapidly away from the centre of the bud with a corresponding flattening of the membrane (figure 13*d*). The value of the membrane tension, which is initially larger at the centre, eventually reduces to its

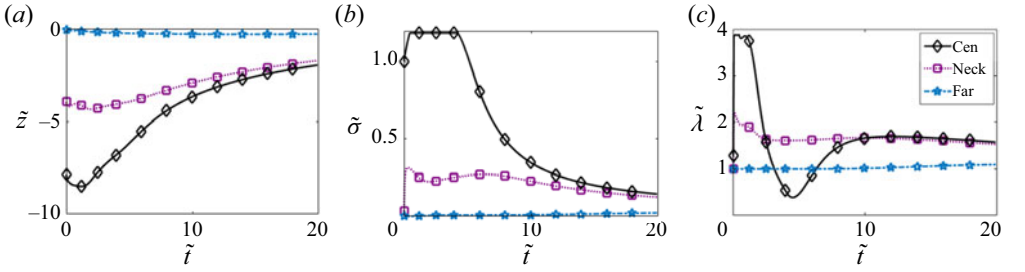

FIGURE 14. Temporal evolution of: (*a*) vertical displacement, (*b*) protein density and (*c*) membrane tension at three different locations: centre of the membrane (cen), neck of the bud (neck) (dimensionless arclength distance from the centre is 4.2) and far from the bud (far) (dimensionless arclength distance from the centre is 14.3).

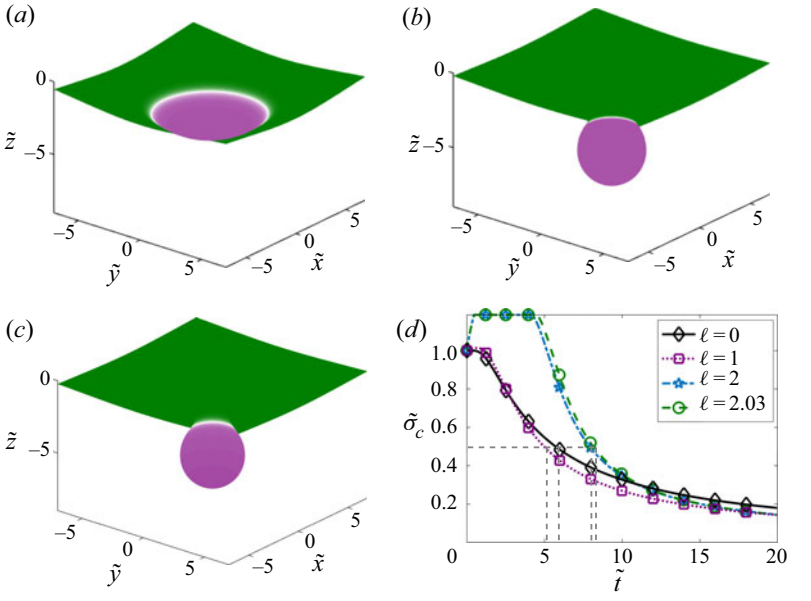

FIGURE 15. Coupling of protein curvature-inducing effect and diffusion. Initial distribution of the protein for (*a*) $\ell = 1$ nm, (*b*) $\ell = 2$ nm and (*c*) $\ell = 2.03$ nm. (*d*) Temporal dynamics of the density of the protein at the centre of the membrane for the three different configurations. The dashed lines highlight the time it takes for $\tilde{\sigma}_c$ to decrease from 1 to 0.5.

boundary value as the protein density becomes uniform (figure 13*e–g*). The flow profile follows the membrane deformation and the protein distribution over time. Initially, the tangential velocity is directed towards the centre causing advection of the protein towards the tip (compare figure 13*h* and figure 13*i*). At later times, as the protein diffuses out and the membrane begins to flatten, the flow direction reverses direction, consistent with the continuity equation (figure 13*j*).

Figure 14 shows the change in the displacement (*a*), protein density (*b*) and membrane tension (*c*) at three different locations: centre of the membrane (centre), neck of the bud (neck) and a location far from the bud (far). We observe that the displacement at the centre of the membrane and at the neck first increases and then decreases consistent with

the initial widening of the neck (figure 14*a*). No observable change in deformation was noted far from the bud. The protein density increases at the centre before decreasing over time (figure 14*b*). We enforced a maximum value of 1.25 for $\tilde{\sigma}$ in the simulations in place of introducing a surface saturation density of proteins on the membrane; this can be interpreted as a simple model for protein crowding. The protein density at the neck remains more or less uniform for a long time, consistent with the diffusion of proteins away from the bud towards the flat membrane. The membrane tension at the centre initially decreases and then increases (figure 14*c*). Recall that the membrane tension is simply the negative of the surface pressure (Steigmann 1999; Rangamani *et al.* 2013, 2014). The drop in the membrane tension corresponds to the change in the direction of the viscous pressure drop that results from the change in direction of the velocity field. Membrane tension increases further as the contribution from the viscous component becomes weak over time and the elastic component dominates. This is consistent with the nature of the membrane tension for the linear Monge case (figure 8*a*).

Finally, we varied the extent of the curvature induced by the protein by varying the characteristic protein size ℓ (figure 15). For a small value of $\ell = 1$ nm such that the initial curvature was a small deviation from the flat plane (figure 15*a*), protein diffusion flattens out the membrane similar to the results observed in the Monge parametrization (figure 7*a*) and for diffusion on a flat surface (figure 12*d*) corresponding to the case where $\ell = 0$. However, increasing ℓ to 2 and 2.03 nm in figure 15(*b*,*c*) such that the initial shape is a well-defined bud leads to an altered temporal dynamics. We compared the time required for $\tilde{\sigma}_c$ to decrease from 1 to 0.5 for different values of ℓ. Interestingly, we find that low curvatures promote slightly faster diffusion of protein from the centre of the domain as compared to flat surfaces (compare $\ell = 0$ to $\ell = 1$ nm). For high values of ℓ, this time scale increases but the flattening of the membrane coupled with diffusion results in similar long-time dynamics, which is different from the case of fixed surface curvature. Thus, we find that the coupling between membrane bending, protein diffusion and lipid flow reveals an intricate and a somewhat counterintuitive relationship, with nonlinear dependencies between protein diffusion timescales and membrane curvature.

5. Conclusions and discussion

In this work, we have derived and analysed the governing equations for the protein-induced deformation of a lipid membrane coupled with protein diffusion and in-plane viscous flow of the lipids. The coupling between diffusion and lipid flow completes the description of the key transport phenomena involved in lipid membranes. We conducted simulations in one dimension and two dimensions (linearized Monge and axisymmetry) and further quantified the relationship between membrane bending and protein diffusion. The major conclusions from our study are that lipid flow and membrane protein diffusion, when coupled, can alter the dynamics of membrane protein distribution at different locations. We find that, as the protein diffuses from an initial locally concentrated patch in the small deformation regime, the membrane deformation decreases and this dynamics is also related to the diffusion coefficient of proteins on the membrane. The flow of lipids also seems to induce a separation dynamics that depends on the Péclet number of the system when multiple patches are present.

In the case of buds, because of the strong coupling between protein diffusion and membrane bending, certain nonlinearities are observed. First, we note that the diffusion of protein at the centre of a bud depends on the extent of curvature induced by the protein. Second, we note that in buds, proteins first tend to move towards the centre of the bud to enable widening of the neck and then diffuse away from the centre. These findings have

implications for membrane flattening after fusion in cellular processes such as exocytosis (Hurley *et al.* 2010) and membrane repair (Blazek, Paleo & Weisleder 2015).

Previously, we elaborated on the need for coupling between the viscous and elastic effects for the calculation of the Lagrange multiplier associated with the incompressibility constraint of the membrane (Rangamani *et al.* 2013, 2014). Here, we build on that framework to include protein diffusion. The coupled interaction between elasticity, diffusion, and viscous flow now fully describes the equations associated with the Lagrange multiplier λ, reinforcing its interpretation as a surface pressure (Rangamani *et al.* 2013; Steigmann 2018). We note that further efforts are needed in simulation technologies such that complex geometries can be simulated (Kumar, Gompper & Lipowsky 2001; Sauer *et al.* 2017; Sahu *et al.* 2020; Vasan *et al.* 2020).

There have been many studies focused on modelling membrane–protein interactions (Stachowiak *et al.* 2010; Lipowsky 2013). Here, we show that coupling the viscous flow of lipids on the membrane is important for modulating the dynamics of the system and fully describing interfacial transport phenomena. Future efforts will focus on adsorption of proteins from the bulk (Glasmaster *et al.* 2002; Zhdanov & Kasemo 2010) and phase separation of proteins to identify the coupling between lipid flow and chemical energies associated with these processes on an elastic membrane. Such theoretical developments not only have implications for our understanding of biological membranes, but also have the potential to impact curvature-driven, directed assembly in colloids and liquid crystals suspended in fluids, and particle interactions at interfaces between immiscible fluids and soft materials, enabling directed design and engineering of the next generation of reconfigurable systems in soft matter (Liu, Sharifi-Mood & Stebe 2018; Anjali & Basavaraj 2019).

Declaration of interests

The authors report no conflict of interest.

Acknowledgements

The authors would like to thank Professor D. Steigmann for initial discussions on the model development. They would also like to thank Mr A. Sahu of UC Berkeley for his critical feedback. This work was supported in part by ONR N00014-17-1-2628 and NIH R01GM132106 to PR, and by NSF CBET-1705377 to DS.

Appendix A. Analytical justification for the flat plane as the equilibrium solution

Our 1-D simulations in § 3.2 show that at steady state the protein distribution reaches a uniform distribution while the string approaches the flat configuration. Here, we rationalize this result and prove theoretically that the flat configuration with uniform protein density is indeed an exact solution. To this end, we consider the arc-length parametrization and write the energy Lagrangian as

$$\mathcal{L} = \int [k(H - C)^2 + \lambda] \, \mathrm{d}s = \int [k(\psi_s - C)^2 + \lambda] \, \mathrm{d}s. \tag{A 1}$$

In the above relation, ψ is the angle made by the string with the horizontal direction and s is the arc length. The curvature, in this case, is given by ψ_s. The tangential force balance

reads

$$2k[\psi_s - C(s)]C'(s) = \lambda_s, \tag{A 2}$$

which provides an equation for the string tension λ for a given shape and spontaneous curvature. For a uniform protein density, the spontaneous curvature is also uniform: $C(s) = C_0$, and (A 2) then implies a uniform tension $\lambda(s) = \lambda_0$ everywhere in the domain. The Lagrangian then simplifies to

$$\mathcal{L} = \int_{-L/2}^{L/2} [(\psi_s - C_0)^2 + \Lambda_0]\mathrm{d}s, \quad \text{with } \Lambda_0 = \frac{\lambda_0}{k}. \tag{A 3}$$

Here, we have taken the domain to be $-L/2 \le s \le L/2$, and we assume the following boundary conditions at both ends:

$$y(-L/2) = y(L/2) = 0, \quad \psi(-L/2) = \psi(L/2) = 0. \tag{A 4a,b}$$

Without loss of generality, we can consider symmetric deformations with respect to $s = 0$, and seek the solution for ψ_s as a Fourier cosine series of the form

$$\psi_s = a_0 + \sum_{n=1}^{\infty} a_n \cos\frac{2n\pi s}{L}. \tag{A 5}$$

Substituting this series into (A 3) yields

$$\begin{aligned}\mathcal{L} &= \int_{-L/2}^{L/2} \left[k\left(a_0 + \sum_{n=1}^{\infty} a_n \cos\frac{2n\pi s}{L} - C_0 \right)^2 + \lambda_0 \right] \mathrm{d}s \\ &= \frac{L}{2}\sum_{n=1}^{\infty} k a_n^2 + L(kC_0^2 + \lambda_0).\end{aligned} \tag{A 6}$$

We find that $\mathcal{L}$ is independent of a_0. Minimizing $\mathcal{L}$ with respect to the Fourier coefficients leads to $a_i = 0$ for $i \neq 0$. We therefore find that $\phi_s = a_0$, which integrates to $\psi = a_0 s + b$. Using the boundary conditions (A 4*a*,*b*), we obtain

$$\psi(s) = 0, \tag{A 7}$$

which indicates that the flat configuration is the equilibrium solution in this case.

Appendix B. Validation of algorithm for pressure-Poisson equation

In § 3, we solved the coupled membrane tension and velocity for the case of linear Monge by solving the pressure-Poisson equation with the help of the integral representation of (3.19). Here, we present a validation of this method and compare the result with the Stokes–Neumann system (Glowinski *et al.* 2005). Recall the governing

equations for the fluid flow in the present case

$$\tilde{\boldsymbol{\nabla}} \cdot \tilde{\boldsymbol{v}} = 2\tilde{w}\tilde{H}, \tag{B 1}$$

$$\begin{aligned} \tilde{\boldsymbol{\nabla}}\tilde{\lambda} + \tilde{\nabla}^2\tilde{\boldsymbol{v}} + \tilde{\boldsymbol{\nabla}}(\tilde{\boldsymbol{\nabla}} \cdot \tilde{\boldsymbol{v}}) - 4\tilde{w}\tilde{\boldsymbol{\nabla}}\tilde{H} - 2\tilde{\boldsymbol{\nabla}}\tilde{w} : \tilde{\boldsymbol{\nabla}}\tilde{\boldsymbol{\nabla}}\tilde{z} \\ = \tilde{\boldsymbol{\nabla}}\tilde{\sigma}\left[\frac{2\hat{C}\hat{B}}{\hat{T}}\tilde{\nabla}^2\tilde{z} - \frac{4\hat{C}^2\hat{B}^2}{\hat{T}}\tilde{\sigma} - \frac{2\hat{C}}{\hat{T}}\log\left(\frac{\tilde{\sigma}}{\tilde{\sigma}_s}\right)\right]. \end{aligned} \tag{B 2}$$

The velocity field $\boldsymbol{v}$ can be written as a Helmholtz decomposition

$$\tilde{\boldsymbol{v}} = \tilde{\boldsymbol{\nabla}}\phi + \tilde{\boldsymbol{\nabla}} \times \tilde{\boldsymbol{\zeta}} = \tilde{\boldsymbol{v}}_d + \tilde{\boldsymbol{u}}, \tag{B 3}$$

where $\tilde{\boldsymbol{v}}_d$ is curl free and $\tilde{\boldsymbol{u}}$ is divergence free. In particular, the continuity equation (B 1) becomes $\tilde{\boldsymbol{\nabla}} \cdot \tilde{\boldsymbol{v}}_d = 2\tilde{w}\tilde{H}$. Now, substituting $\tilde{\boldsymbol{v}} = \tilde{\boldsymbol{u}} + \tilde{\boldsymbol{v}}_d$ into the governing equations (B 1)–(B 2) for the fluid flow yields the modified system of equations

$$\tilde{\boldsymbol{\nabla}} \cdot \tilde{\boldsymbol{u}} = 0, \tag{B 4}$$

$$\tilde{\boldsymbol{\nabla}}\tilde{\lambda} + \tilde{\nabla}^2\tilde{\boldsymbol{u}} + \tilde{\boldsymbol{f}} = 0, \tag{B 5}$$

where,

$$\begin{aligned} \tilde{\boldsymbol{f}} = 2\tilde{\boldsymbol{\nabla}}(2\tilde{w}\tilde{H}) - 4\tilde{w}\tilde{\boldsymbol{\nabla}}\tilde{H} - 2\tilde{\boldsymbol{\nabla}}\tilde{w} : \tilde{\boldsymbol{\nabla}}\tilde{\boldsymbol{\nabla}}\tilde{z} \\ - \tilde{\boldsymbol{\nabla}}\tilde{\sigma}\left[\frac{2\hat{C}\hat{B}}{\hat{T}}\tilde{\nabla}^2\tilde{z} - \frac{4\hat{C}^2\hat{B}^2}{\hat{T}}\tilde{\sigma} - \frac{2\hat{C}}{\hat{T}}\log\left(\frac{\tilde{\sigma}}{\tilde{\sigma}_s}\right)\right]. \end{aligned} \tag{B 6}$$

Equations (B 5)–(B 4) constitute a non-homogeneous Stokes problem with body force $\tilde{\boldsymbol{f}}$. We solve it here with boundary conditions $\tilde{\boldsymbol{u}}_\infty \to \boldsymbol{0}$ and $\widetilde{\lambda}_\infty \to 1$ at infinity. In that case, the velocity and pressure are simply obtained using the boundary integral equations (Pozrikidis 1992)

$$\tilde{\boldsymbol{u}}(\tilde{\boldsymbol{x}}) = \int_\Omega \boldsymbol{\mathcal{G}}(\tilde{\boldsymbol{x}} - \tilde{\boldsymbol{x}}_0) \cdot \boldsymbol{f}(\boldsymbol{x}_0)\,\mathrm{d}A(\tilde{\boldsymbol{x}}_0), \tag{B 7}$$

$$\tilde{\lambda}(\tilde{\boldsymbol{x}}) = 1 + \int_\Omega \boldsymbol{\Pi}(\tilde{\boldsymbol{x}} - \tilde{\boldsymbol{x}}_0) \cdot \boldsymbol{f}(\boldsymbol{x}_0)\,\mathrm{d}A(\tilde{\boldsymbol{x}}_0), \tag{B 8}$$

where $\boldsymbol{\mathcal{G}}$ and $\boldsymbol{\Pi}$ are the velocity and pressure Green's functions for two-dimensional Stokes flow and are given by

$$\left.\begin{aligned} \boldsymbol{\mathcal{G}}(\tilde{\boldsymbol{x}}) &= \frac{1}{4\pi}\left(\frac{\tilde{\boldsymbol{x}}\tilde{\boldsymbol{x}}}{|\tilde{\boldsymbol{x}}|^2} - \boldsymbol{I}\log|\tilde{\boldsymbol{x}}|\right), \\ \boldsymbol{\Pi}(\tilde{\boldsymbol{x}}) &= -\frac{1}{2\pi}\frac{\tilde{\boldsymbol{x}}}{|\tilde{\boldsymbol{x}}|^2}. \end{aligned}\right\} \tag{B 9}$$

Figure 16 compares the membrane tension profile $\widetilde{\lambda}$ obtained in figure 3(*a*) for a single patch with the solution obtained using the Stokes–Neumann formalism. We find that the relative error is well below 4 % everywhere in the domain (*a*). The two membrane tension profiles overlap over most of the domain except for a small deviation near the centre (*b*).

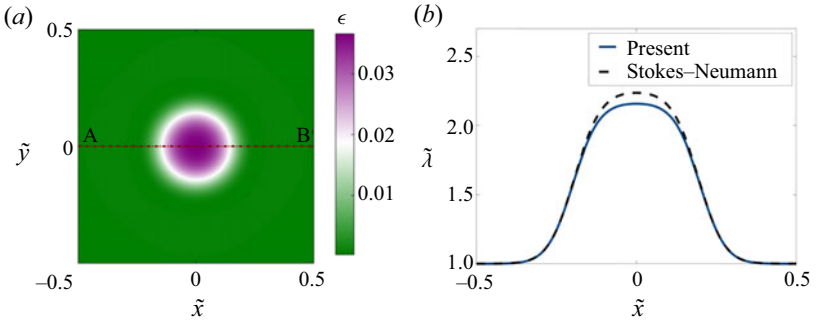

FIGURE 16. Comparison between membrane tension calculated using the present model and a Stokes–Neumann formulation (Glowinski *et al.* 2005). (*a*) Relative error $\epsilon = (\lambda - \lambda_{SN})/\lambda_{SN}$ in the membrane tension for the case of single patch of protein (figure 3*a*) at time $\tilde{t} = 5 \times 10^{-3}$. (*b*) Membrane tension distribution along line AB shown in (*a*) for the present model and Stokes–Neumann solution.

REFERENCES

ALBERTS, B., JOHNSON, A., LEWIS, J., RAFF, M., ROBERTS, K. & WALTER, P. 1985 *Molecular Biology of the Cell*. Garland Science.

ALIMOHAMADI, H. & RANGAMANI, P. 2018 Modeling membrane curvature generation due to membrane–protein interactions. *Biomolecules* **8**, 120–147.

ANJALI, T. G. & BASAVARAJ, M. G. 2019 Shape-anisotropic colloids at interfaces. *Langmuir* **35**, 3–20.

ANTONNY, B. 2011 Mechanisms of membrane curvature sensing. *Annu. Rev. Biochem.* **80**, 101–123.

ARIS, R. 1989 *Vectors, Tensors and Basic Equation of Fluid Mechanics*. Dover.

ARROYO, M. & DESIMONE, A. 2009 Relaxation dynamics of fluid membranes. *Phys. Rev.* E **79**, 031915.

ARROYO, M., WALANI, N., TORRES-SANCHEZ, A. & KAURIN, D. 2018 Onsager's variational principle in soft matter: introduction and application to the dynamics of adsorption of proteins onto fluid membranes. In *The Role of Mechanics in the Study of Lipid Bilayers* (ed. D. J. Steigmann), pp. 1–53. Springer.

BAHMANI, F., CHRISTENSON, J. & RANGAMANI, P. 2016 Analysis of lipid flow on minimal surfaces. *Contin. Mech. Thermodyn.* **28**, 503–513.

BASSEREAU, P., JIN, R., BAUMGART, T., DESERNO, M., DIMOVA, R., FROLOV, V. A., BASHKIROV, P. V., GRUBMÜLLER, H., JAHN, R. & RISSELADA, H. J. *et al.* 2018 The 2018 biomembrane curvature and remodeling roadmap. *J. Phys.* D*: Appl. Phys.* **51**, 343001.

BAUMGART, T., HESS, S. T. & WEBB, W. W. 2003 Imaging coexisting fluid domains in biomembrane models coupling curvature and line tension. *Nature* **425**, 821–824.

BLAZEK, A. D., PALEO, B. J. & WEISLEDER, N. 2015 Plasma membrane repair: a central process for maintaining cellular homeostasis. *Physiology* **30**, 438–448.

CAMPELO, F. & HERNÁNDEZ-MACHADO, A. 2007 Model for curvature-driven pearling instability in membranes. *Phys. Rev. Lett.* **99**, 088101.

CANHAM, P. B. 1970 The minimum energy of bending as a possible explanation of the biconcave shape of the human red blood cell. *J. Theor. Biol.* **26**, 61–81.

CHABANON, M. & RANGAMANI, P. 2018 Gaussian curvature directs the distribution of spontaneous curvature on bilayer membrane necks. *Soft Matt.* **12**, 2281–2294.

CHABANON, M. & RANGAMANI, P. 2019 Geometric coupling of helicoidal ramps and curvature-inducing proteins in organelle membranes. *J. R. Soc. Interface* **16**, 20190354.

DANNHAUSER, P. N. & UNGEWICKELL, E. J. 2012 Reconstitution of clathrin-coated bud and vesicle formation with minimal components. *Nat. Cell Biol.* **14**, 634–639.

DO, C. 1976 *Differential Geometry of Curves and Surfaces*. Prentice Hall.

ELLIOTT, C. M., GRASER, C., HOBBS, G., KORNHUBER, R. & WOLF, M. A. 2016 A variational approach to particles in lipid membranes. *Arch. Rat. Mech. Anal.* **222**, 1011–1075.

ELLIOTT, C. M. & STINNER, B. 2013 Computation of two-phase biomembranes with phase dependent material parameters using surface finite elements. *Commun. Comput. Phys.* **13**, 325–360.

GERA, P. & SALAC, D. 2017 Cahn–Hilliard on surfaces: a numerical study. *Appl. Math. Lett.* **73**, 56–61.

GLASMASTER, K., LARSSON, C., HOOK, F. & KASEMO, B. 2002 Protein adsorption on supported phospholipid bilayer. *J. Colloid Interface Sci.* **246**, 40–47.

GLOWINSKI, R., PAN, T.-W., JUAREZ, V. L. H. & DEAN, E. 2005 Numerical methods for the simulation of incompressible viscous flow: an introduction. In *Multidisciplinary Methods for Analysis Optimization and Control of Complex Systems* (ed. V. Capasso & J. Périaux), pp. 49–175. Springer.

GOV, N. S. 2018 Guided by curvature: shaping cells by coupling curved membrane proteins and cytoskeletal forces. *Phil. Trans. R. Soc. Lond.* B **373**, 20170115.

GOZDZ, W. T. 2011 Shape transformation of lipid vesicle induced by diffusing macromolecules. *J. Chem. Phys.* **134**, 371–379.

GÓŹDŹ, W. T. & GOMPPER, G. 1998 Composition-driven shape transformations of membranes of complex topology. *Phys. Rev. Lett.* **80**, 4213–4216.

GRUENBERG, J. 2001 The endocytic pathway: A mosaic of domains. *Nat. Rev. Mol. Cell Biol.* **2**, 721–730.

HARAYAMA, T. & RIEZMAN, H. 2018 Understanding the diversity of membrane lipid composition. *Nat. Rev. Mol. Cell Biol.* **19**, 281–296.

HASSINGER, J. E., OSTER, G., DRUBIN, D. G. & RANGAMANI, P. 2017 Design principles for robust vesiculation in clathrin-mediated endocytosis. *Proc. Natl Acad. Sci. USA* **114**, 1118–1127.

HAUCKE, V. & KOZLOV, M. M. 2018 Membrane remodeling in clathrin-mediated endocytosis. *J. Cell Sci.* **131**, jcs216812.

HELFRICH, W. 1973 Elastic properties of lipid bilayers: theory and possible experiments. *Z. Naturforsch.* C **5**, 693–703.

HORNER, A., ANTONENKO, Y. N. & POHL, P. 2009 Coupled diffusion of peripherally bound peptides along the outer and inner membrane leaflets. *Biophys. J.* **96**, 2689–2695.

HURLEY, J. H., BOURA, E., CARLSON, L.-A. & RÓŻYCKI, B. 2010 Membrane budding. *Cell* **143**, 875–887.

IGLIČ, A., BABNIK, B., GIMSA, U. & KRALJ-IGLIČ, V. 2005 On the role of membrane anisotropy in the beading transition of undulated tubular membrane structures. *J. Phys.* A **40**, 8527–8536.

JAHN, R., LANG, T. & SÜDHOF, T. C. 2003 Membrane fusion. *Cell* **112**, 519–533.

JENKINS, J. T. 1977 The equation of mechanical equilibrium of a model membrane. *SIAM J. Appl. Maths* **4**, 693–703.

JÜLICHER, F. & LIPOWSKY, R. 1993 Domain-induced budding of vesicles. *Phys. Rev. Lett.* **70**, 2964–2967.

KAHYA, N., SCHERFELD, D., BACIA, K. & SCHWILLE, P. 2004 Lipid domain formation and dynamics in giant unilamellar vesicles explored by fluorescence correlation spectroscopy. *J. Struct. Biol.* **147**, 77–89.

KOZLOVSKY, Y. & KOZLOV, M. M. 2003 Membrane fission: model for intermediate structures. *Biophys. J.* **85**, 85–96.

KRALJ-IGLIČ, V., HAGERSTAND, H., VERANIC, P., JEZERNIK, K., BABNIK, B., GAUGER, D. R. & IGLIČ, A. 2005 Amphiphile-induced tubular budding of the bilayer membrane. *Eur. Biophys. J.* **34**, 1066–1070.

KREYSZIG, E. 1968 *Advanced Engineering Mathematics*. Wiley.

KUMAR, P. B. S., GOMPPER, G. & LIPOWSKY, R. 2001 Budding dynamics of multicomponent membranes. *Phys. Rev. Lett.* **86**, 3911.

LEIBLER, S. & ANDELMAN, D. 1987 Ordered and curved meso-structures in membranes and amphiphilic films. *J. Phys. France* **48**, 2013–2018.

LIPOWSKY, R. 1991 The conformation of membranes. *Nature* **349**, 475–481.

LIPOWSKY, R. 2013 Spontaneous tubulation of membranes and vesicles reveals membrane tension generated by spontaneous curvature. *Faraday Discuss.* **161**, 305–331.

LIU, I. B., SHARIFI-MOOD, N. & STEBE, K. J. 2018 Capillary assembly of colloids: interactions on planar and curved interfaces. *Annu. Rev. Condens. Matter Phys.* **9**, 283–305.

LOWENGRUB, J. S., RATZ, A. & VOIGT, A. 2009 Phase-field modeling of the dynamics of multicomponent vesicles: spinodal decomposition, coarsening, budding, and fission. *Phys. Rev.* E **79**, 031926.

MCMAHON, H. T. & GALLOP, J. L. 2005 Membrane curvature and mechanisms of dynamic cell membrane remodeling. *Nature* **438**, 590–596.

MIETKE, A., JULICHER, F. & SBALZARINI, I. F. 2019 Self-organized shape dynamics of active surfaces. *Proc. Natl Acad. Sci. USA* **116**, 29–34.

MIKUCKI, M. & ZHOU, Y. C. 2017 Curvature-driven molecular flow on membrane surface. *SIAM J. Appl. Math.* **77**, 1587–1605.

MUJHERJEE, S. & MAXFIELD, E. R. 2000 Role of membrane organization and membrane domains in endocytic lipid trafficking. *Traffic* **1**, 203–211.

NITSCHKE, I, VOIGT, A & WENSCH, J 2012 A finite element approach to incompressible two-phase flow on manifolds. *J. Fluid Mech.* **708**, 418–438.

NOGUCHI, H. & GOMPPER, G. 2004 Fluid vesicles with viscous membranes in shear flow. *Phys. Rev. Lett.* **93**, 258102.

POZRIKIDIS, C. 1992 *Boundary Integral and Singularity Methods for Linearized Viscous Flow*. Cambridge University Press.

RAHIMI, M. & ARROYO, M. 2012 Shape dynamics, lipid hydrodynamics, and complex viscoelasdticity of bilayer membranes. *Phys. Rev.* E **86**, 011932.

RAMASWAMY, S., TONER, J. & PROST, J. 2005 Nonequilibrium fluctuations, travelling waves, and instabilities in active membranes. *Phys. Rev. Lett.* **84**, 3494–3497.

RANGAMANI, P., AGRAWAL, A., MANDADAPU, K., OSTER, G. & STEIGMANN, D. 2013 Interaction between surface shape and intra-surface viscous flow on lipid membranes. *Biomech. Model. Mechanobiol.* **12**, 833–845.

RANGAMANI, P., BEHZADAN, A. & HOLST, M. 2020 Local sensitivity analysis of the 'membrane shape equation' derived from Helfrich energy. arXiv:2005.12550.

RANGAMANI, P., MANDADAPU, K. & OSTER, G. 2014 Protein induced membrane curvature alters local membrane tension. *Biophys. J.* **107**, 751–762.

REYNWAR, B. J., ILLYA, G., HARMANDARIS, V. A., MÜLLER, M. M., KREMER, K. & DESERNO, M. 2007 Aggregation and vesiculation of membrane proteins by curvature-mediated interactions. *Nature* **447**, 461–464.

SACKMANN, E., DUWE, H. P. & ENGELHARDT, H. 1986 Membrane bending elasticity and its role for shape fluctuations and shape transformations of cells and vesicles. *Faraday Discuss. Chem. Soc.* **81**, 281–290.

SAHU, A., OMAR, Y. A. D., SAUER, R. A. & MANDADAPU, K. K. 2020 Arbitrary Lagrangian–Eulerian finite element method for curved and deforming surfaces: I. General theory and application to fluid interfaces. *J. Comput. Phys.* **407**, 109253.

SAHU, A., SAUER, R. A. & MANDADAPU, K. K. 2017 Irreversible thermodynamics of curved lipid membranes. *Phys. Rev.* E **96**, 042409.

SALBREUX, G. & JÜLICHER, F. 2017 Mechanics of active surfaces. *Phys. Rev.* E **96**, 032404.

SAUER, R. A., DUONG, T. X., MANDADAPU, K. K. & STEIGMANN, D. J. 2017 A stabilized finite element formulation for liquid shells and its application to lipid bilayers. *J. Comput. Phys.* **330**, 436–466.

SCRIVEN, L. E. 1960 Dynamics of a fluid surface. *Chem. Engng Sci.* **12**, 98–108.

SEIFERT, U. 1993 Curvature-induced lateral phase segregation in two-component vesicles. *Phys. Rev. Lett.* **70**, 1335–1338.

SEIFERT, U. & LANGER, S. A. 1993 Viscous modes of fluid bilayer membranes. *Europhys. Lett.* **23**, 65–72.

SINGER, S. 1974 The molecular organization of membranes. *Annu. Rev. Biochem.* **43**, 805–833.

SNEAD, W. T., HAYDEN, C. C., GADOK, A. K., ZHAO, C., LAFER, E. M., RANGAMANI, P. & STACHOWIAK, J. C. 2017 Membrane fission by protein crowding. *Proc. Natl Acad. Sci.* **114**, 3258–3267.

SOKOLNIKOFF, I. S. 1951 *Tensor Analysis: Theory and Applications*. Wiley.

STACHOWIAK, J. C., HAYDEN, C. C. & SASKI, D. Y. 2010 Steric confinement of proteins on lipid membranes can drive curvature and tubulation. *Proc. Natl Acad. Sci.* **107**, 7781–7786.

STEIGMANN, D. & AGRAWAL, A. 2011 A model for surface diffusion of trans-membrane protein on lipid bilayers. *Z. Angew. Math. Phys.* **62**, 449–563.

STEIGMANN, D., BAESU, E., RUDD, R. E., BELAK, J. & MCELERESH, M. 2003 On the variational theory of cell-membrane equilibria. *Interface. Free Bound.* **5**, 357–366.

STEIGMANN, D. J. 1999 Fluid films with curvature elasticity. *Arch. Rat. Mech. Anal.* **150**, 257–272.

STEIGMANN, D. J. 2018 Mechanics and physics of lipid bilayers. In *The Role of Mechanics in the Study of Lipid Bilayers* (ed. D. J. Steigmann), pp. 1–61. Springer.

TORRES-SANCHEZ, A., MILLAN, D. & ARROYO, M. 2019 Modelling fluid deformable surfaces with an emphasis on biological interfaces. *J. Fluid Mech.* **872**, 218–271.

TOZZI, C., WALANI, N. & ARROYO, M. 2019 Out-of-equilibrium mechanochemistry and self-organization of fluid membranes interacting with curved proteins. *New J. Phys.* **21**, 093004.

TRAN-SON-TAY, R., SUTERA, S. P. & RAO, P. R. 1984 Determination of red blood cell membrane viscosity from rheoscopic observations of tank-treading motion. *Biophys. J.* **46**, 1335–1338.

VASAN, R., RUDRARAJU, S., AKAMATSU, M., GARIKIPATI, K. & RANGAMANI, P. 2020 A mechanical model reveals that non-axisymmetric buckling lowers the energy barrier associated with membrane neck constriction. *Soft Matt.* **16**, 784–797.

VEKSLER, A. & GOV, N. S. 2007 Phase transitions of the coupled membrane-cytoskeleton modify cellular shape. *Biophys. J.* **93**, 3798–3810.

ZHDANOV, V. P. & KASEMO, B. 2010 Adsorption of proteins on a lipid bilayer. *Eur. Biophys. J.* **39**, 1477–1482.

ZHONG-CAN, O.-Y. & HELFRICH, W. 1989 Bending energy of vesicle membranes: general expressions for the first, second, and third variation of the shape energy and applications to spheres and cylinders. *Phys. Rev.* A **39**, 5280–5288.

ZIMMERBERG, J. & KOZLOV, M. M. 2006 How proteins produce cellular membrane curvature. *Nat. Rev. Mol. Cell Biol.* **7**, 9–19.